Computationally generated maps of surface structures and catalytic activities for alloy phase diagrams

Liang Cao[a], Le Niu[a], and Tim Mueller[a,*]

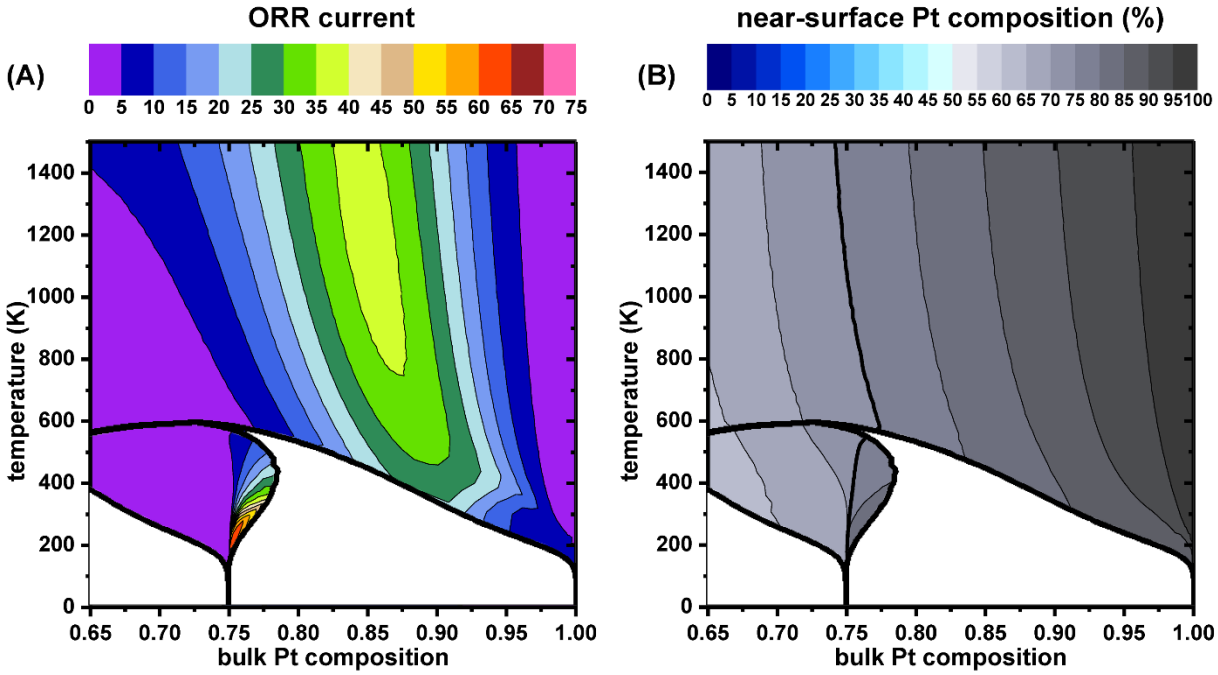

[a]Department of Materials Science and Engineering, Johns Hopkins University, Baltimore, MD 21218, USA

*Corresponding Author
Tim Mueller
Department of Materials Science and Engineering
Johns Hopkins University
3400 N. Charles St.
Baltimore, MD 21218 USA
(410) 516-5779
tmueller@jhu.edu

Abstract

To facilitate the rational design of alloy catalysts, we introduce a method for rapidly calculating the structure and catalytic properties of a substitutional alloy surface that is in equilibrium with the underlying bulk phase. We implement our method by developing a way to generate surface cluster expansions that explicitly account for the lattice parameter of the bulk structure. This approach makes it possible to computationally map the structure of an alloy surface and statistically sample adsorbate binding energies at every point in the alloy phase diagram. When combined with a method for predicting catalytic activities from adsorbate binding energies, maps of catalytic activities at every point in the phase diagram can be created, enabling the identification of synthesis conditions likely to result in highly active catalysts. We demonstrate our approach by analyzing Pt-rich Pt–Ni catalysts for the oxygen reduction reaction, finding two regions in the phase diagram that are predicted to result in highly active catalysts. Our analysis indicates that the $Pt_3Ni(111)$ surface, which has the highest known specific activity for the oxygen reduction reaction, is likely able to achieve its high activity through the formation of an intermetallic phase with $L1_2$ order. We use the generated surface structure and catalytic activity maps to demonstrate how the intermetallic nature of this phase leads to high catalytic activity and discuss how the underlying principles can be used in catalysis design. We further discuss the importance of surface phases and demonstrate how they can dramatically affect catalytic activity.

Keywords: catalyst, design, intermetallic, oxygen reduction reaction, density functional theory, cluster expansion, alloy, strain effect, ensemble effect

Significance Statement

Designing new alloy catalysts is challenging because of the large number of ways the atoms in an alloy can be arranged. We have developed a method that allows researchers to rapidly predict the near-surface atomic arrangement and catalytic properties of an alloy, making it possible to identify the conditions under which alloys should be synthesized to create the best catalysts. We demonstrate our approach by providing evidence that the $Pt_3Ni(111)$ surface, one of the best catalysts for an important reaction in fuel cells, likely draws it excellent catalytic properties from the formation of an alloy phase in which the Pt and Ni atoms are well ordered. These results will facilitate the rational design of new alloy catalysts.

Introduction

Rational design of alloy catalysts is a longstanding goal of chemical engineers and materials scientists (1-6). To design an alloy surface with high catalytic activity it is necessary to account for the lattice parameter of the underlying material (the strain effect) as well as the local atomic structure near each catalytically active site. In the interest of both synthesizability and catalyst durability it is also important to consider the stability of the surface; in alloys that allow substitutional disorder, this typically requires accurately evaluating the energies of a large number of competing surface structures and ensuring that the surface and the underlying bulk material are in equilibrium. Simultaneously accounting for all of these factors presents a significant challenge for computational researchers, especially considering the combinatorial explosion in the number of possible structures in alloys that allow substitutional disorder.

We have developed an approach for addressing this problem that allows for the rapid computational assessment of the structure and activity of the surface of a substitutional alloy. In our approach we use a two-dimensional slab to represent the surface of the alloy and calculate the properties of the slab using cluster expansions (7) trained on density functional theory (DFT) (8) calculations. We introduce a method to generate slab cluster expansions that explicitly depend on the lattice parameter, which allows us to identify surface phases that are in equilibrium with the underlying bulk material by ensuring that the lattice parameters, temperatures, and chemical potentials of all components of the slab match those of the underlying bulk phase. By statistically sampling adsorbate binding energies and using the results in volcano plots (9) to estimate catalytic activity, we are able to generate maps of catalytic activity at all points in the alloy phase diagram. These maps, along with similar maps of surface structure, can be used to interpret experimental results and to guide synthesis efforts to identify

stable surfaces with high catalytic activity. Details of our approach are provided in the Methodology section at the end of this article.

We demonstrate our approach on the (111) surfaces of Pt–Ni alloys, which have drawn much attention as promising catalysts for the oxygen reduction reaction (ORR) at the cathode of fuel cells (10). In 2007 specific activity of 18 mA/cm^2 (about 10 times that of a pure Pt surface) was demonstrated on a Pt-rich $Pt_3Ni(111)$ surface (11). Despite extensive efforts (10), this level of activity has not been achieved by any other catalyst. Previous computational studies have shown that the catalytic activity of the $Pt_3Ni(111)$ surface is strongly influenced by the arrangement of near-surface atoms (5, 12, 13). Through the creation of surface structure maps and a catalytic activity map, we propose that the high catalytic activity of the Pt_3Ni catalyst was likely due to partial formation of the intermetallic Pt_3Ni phase, which resulted in a relatively high Pt concentration in the second layer of the surface. Our results suggest that it may be possible to improve upon this activity through the synthesis of more well-ordered and/or Pt-rich Pt_3Ni materials which are thermodynamically stable but may be challenging to synthesize. Through an analysis of the Pt–Ni system we illustrate some of the benefits of intermetallic phases, which have demonstrated good catalytic properties in other systems (14, 15), as well as the importance of surface phases, which can have dramatic effects on catalytic activity. Although these concepts are illustrated for Pt–Ni and the ORR, they are applicable to alloy catalysts for a variety of chemical reactions.

Results and Discussion

We used a bulk Pt–Ni cluster expansion to predict the Pt-rich side of a Pt–Ni phase diagram (Fig. 1). The calculated phase diagram shows a Pt_3Ni phase with $L1_2$-type order that transitions

to a disordered phase around 600 K. The existence of the $L1_2$-ordered Pt_3Ni phase is in good agreement with experimental results (16, 17) and previous computational results (18-20) including our own work on Pt–Ni nanoparticles (21-23). The shape of the Pt_3Ni region is similar to that in a Pt–Ni phase diagram generated by Lu et al. using the CALPHAD method (18). The order-disorder transition temperature predicted by the cluster expansion (~600 K) is lower than that predicted by the CALPHAD method (~750 K) but close to the experimentally-determined temperature range of 650-690 K (16, 17).

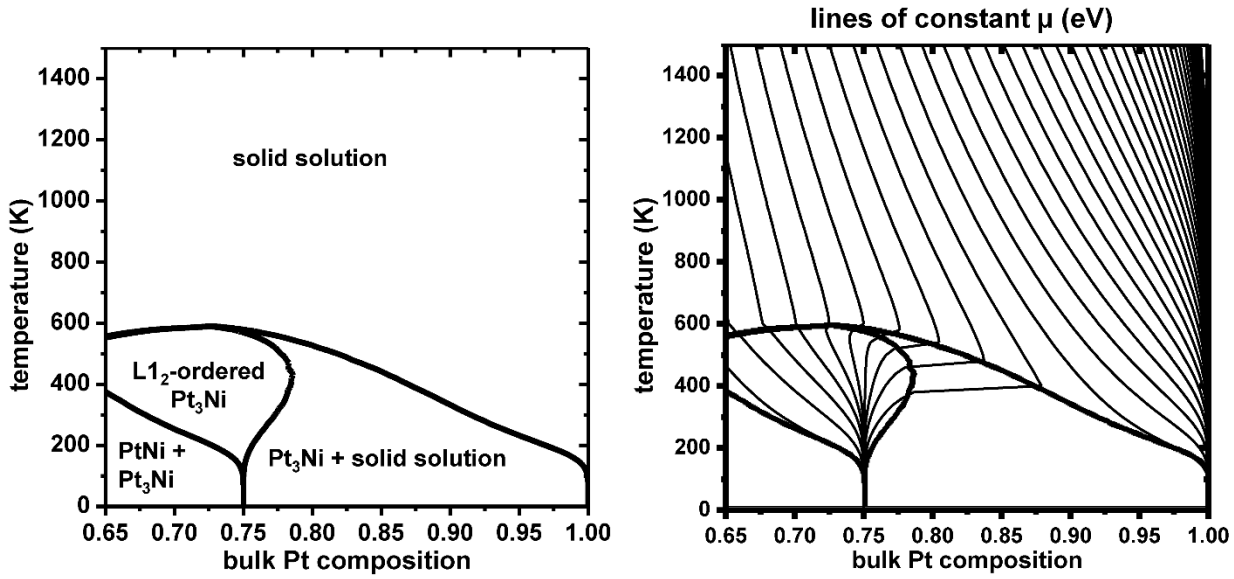

Fig. 1. (A) The predicted bulk Pt-Ni phase diagram. (B) Lines of constant chemical potential (μ, defined in Eq. [4]) ranging from 0.1 eV to 0.9 eV with an increment of 0.02 eV. Connecting chemical potential lines are provided in the two-phase region for clarity.

In nearly all regions of the phase diagram shown in Fig. 1, exposure to oxygen at 0.21 atm pressure and room temperature is predicted to drive segregation of Ni to the surface (*SI Appendix* section 2.3). Thus the as-synthesized surfaces are likely to be metastable upon exposure to oxygen. The degree to which these metastable surfaces retain their structure in practice depends on the nature and environment of the catalyst; the Pt_3Ni catalyst reported by Stamenkovic et al.

was reported to be stable in the potential range of 0.05–1.0 V vs. the reversible hydrogen electrode (RHE) (11), whereas in a (111) layered Pt–Ni–Pt surface structure on bulk Pt, half of the Ni atoms were estimated to segregate to the surface upon oxidation in about 37 minutes at 353 K (24, 25). In the present study we do not evaluate the segregation rates and degree of metastability, focusing instead on the structures and properties of the as-synthesized surfaces.

We calculate the catalytic activities only in the single-phase regions of the phase diagram, as we expect the catalytic activity in two-phase regions will likely be a linear average of the catalytic activities of the two phases present. However we note the possibility that one of the two phases may preferentially form on the surface. The resulting catalytic activity map (Fig. 2A) shows activities that are likely higher than those that can be achieved in practice, as we calculate activity using a Sabatier volcano (9, 26, 27), which is sharply peaked (*SI Appendix* section 2.4). When coverage and kinetics are taken into account, the peak of the volcano plot is likely curved, reducing peak catalytic activities (28, 29). Using kinetic Monte Carlo simulations (*SI Appendix* section 2.6), we have estimated the effects of coverage under the assumption that O is the only species present on the surface (*SI Appendix* Fig. S6). We find that the pattern of activity is similar to that obtained using the Sabatier volcano, but predicted activities do decrease significantly. An improved estimate might be obtained by building a more extensive model that explicitly includes other species, such as OH, that are likely to be present on the surface.

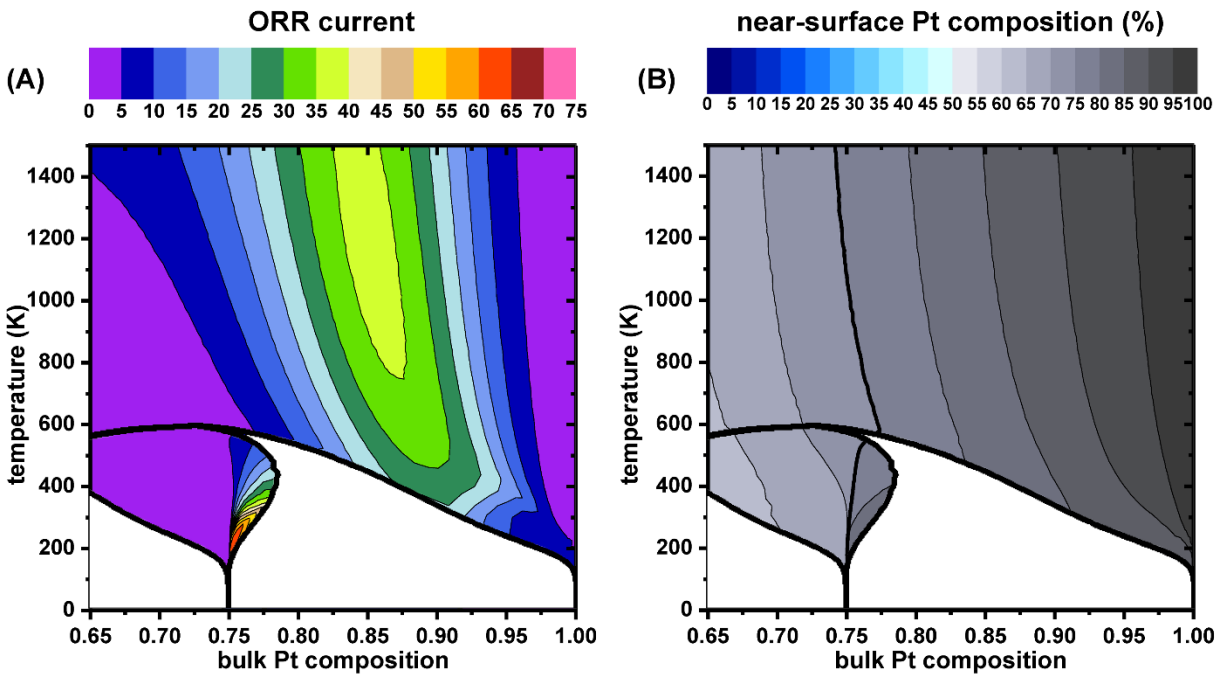

Fig. 2. Catalytic activity and near-surface composition maps for the (111) surfaces of Pt–Ni alloys. (A) The predicted average ORR currents at 298 K relative to Pt(111). (B) The near-surface (top four layers) Pt composition as a function of bulk Pt composition and temperature. Thick black lines mark surface Pt compositions that are multiples of 0.25. The calculated bulk phase diagram in Fig. 1 has been overlaid on figures A and B.

The calculated catalytic activity map reveals two regions in the phase diagram in which the room-temperature catalytic activity is predicted to reach a local maximum. The first, with a maximum activity of about 36 times that of pure Pt(111), occurs in the solid-solution region of the phase diagram at a temperature of about 1200 K and a composition of about 85.4% Pt. This suggests that synthesizing a Pt–Ni alloy under these conditions and quenching to room temperature could result in a highly active catalyst. The global maximum in catalytic activity is predicted to occur for slightly Pt-rich Pt_3Ni at low temperatures, consistent with the catalyst reported by Stamenkovic et al. (11), which was bulk Pt_3Ni with 78.33% Pt in the first three layers. In particular, we find that at a composition of 76.9% Pt and a temperature of 420 K, the bulk composition and predicted near-surface composition profile closely match those of the

experimentally-synthesized catalyst (Fig. 3 and Fig. 4A). The catalytic activity at this point in the phase diagram is predicted to be about 19.6 times that of pure Pt(111). This is larger than the activity observed by Stamenkovic et al. (about 10 times that of Pt(111)), which may again be partially due to our use of a Sabatier volcano.

The predicted composition profile that most closely matches that of the record-setting catalyst is in the ordered (i.e. intermetallic) region of the phase diagram, suggesting that this catalyst was at least partially ordered. In the solid solution (i.e. disordered) phase, the cluster expansion predicts that for bulk compositions near Pt_3Ni the 2nd-layer Pt composition would reach the experimentally observed value for the record-setting catalyst at a temperature of over 1200 K (Fig. 3B). At this temperature there is already predicted to be significant Ni content in the surface layer at a composition of Pt_3Ni (Fig. 3A), which was not reported for the record-setting catalyst (11). It may also be difficult to kinetically trap the material in a structure achieved by annealing at 1200 K. Although it is possible that we underestimate the 2nd-layer Pt content in the solid solution phase, it would be surprising if the optimal composition for a fully disordered material were stoichiometric Pt_3Ni, as there is nothing special about this composition in a solid solution other than that it is the Pt-rich composition that maximizes the thermodynamic driving force for atomic ordering.

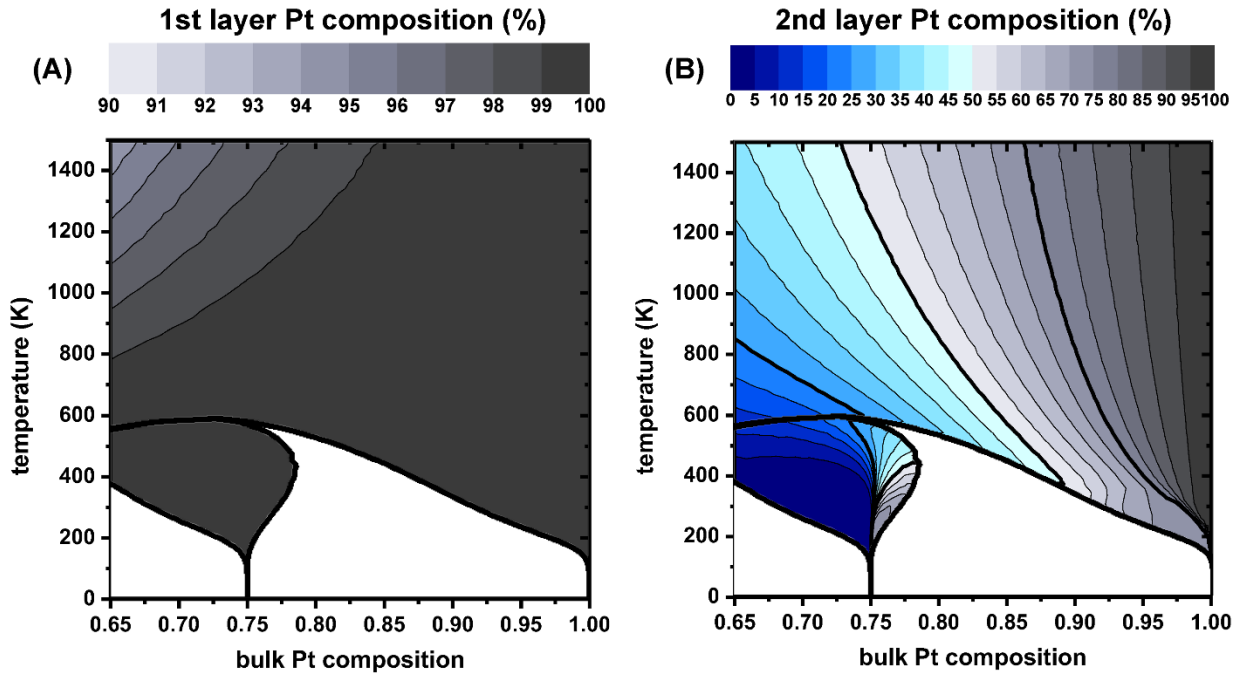

Fig. 3. Layer-by-layer composition maps on slabs. The predicted Pt compositions in the (A) first and (B) second layers of Pt–Ni(111) surfaces as a function of bulk Pt composition and temperature. Thick black lines mark Pt compositions that are multiples of 0.25. The third and fourth layers are shown in *SI Appendix* Fig. S4.

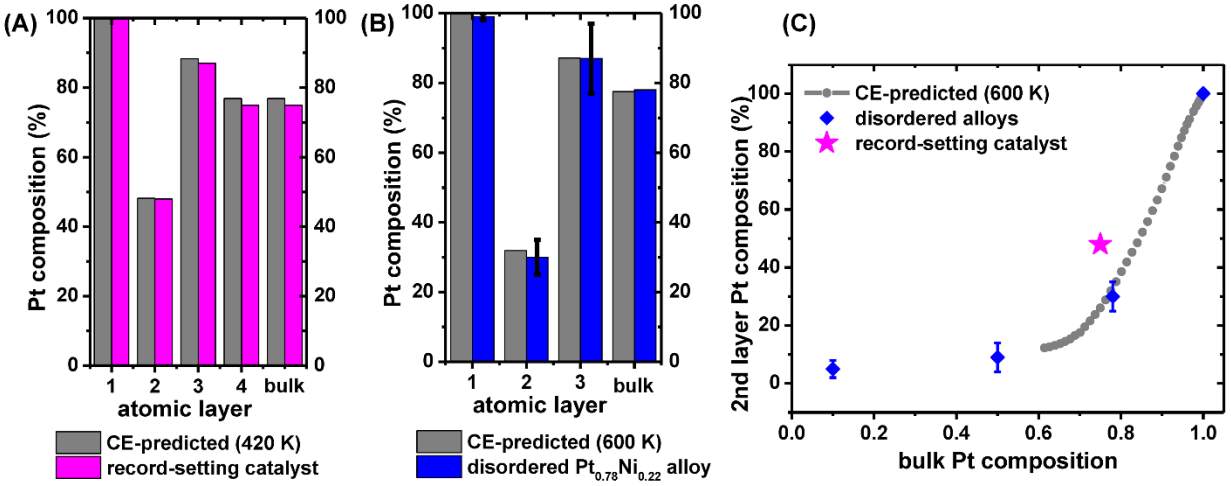

Fig. 4. Comparisons between the cluster-expansion-predicted (CE-predicted) and experimental composition profiles. (A) The predicted layer-by-layer Pt compositions at a temperature of 420 K, closely matching the composition profile for the record-setting catalyst (11). (B) The predicted layer-by-layer Pt compositions at a temperature of 600 K and bulk Pt composition of 77.5%, closely matching the composition profile for disordered $Pt_{0.78}Ni_{0.22}$ (30). (C) The 2nd layer Pt composition in solid solution. The grey dots were predicted by cluster expansion at a temperature of 600 K, and the blue diamonds are experimental values for $Pt_{0.1}Ni_{0.9}$ (31), $Pt_{0.5}Ni_{0.5}$

(30), and $Pt_{0.78}Ni_{0.22}$ (30) (pure Pt is included as well). The magenta star represents the record-setting Pt_3Ni catalyst.

Further evidence that the record-setting Pt_3Ni catalyst was at least partially ordered can be found by comparing its 2nd-layer composition with that of Pt–Ni solid solutions at different bulk compositions. $Pt_{0.78}Ni_{0.22}$ annealed at 1173 K and cooled to room temperature was reported to have a 2nd-layer composition of 30 ± 5% Pt (30). We find that the near-surface composition profile reported in experiments closely matches that predicted by the cluster expansion at a temperature of 600 K (Fig. 4B), suggesting that the material became kinetically trapped around this temperature when cooling. Comparisons with similar experiments for $Pt_{0.1}Ni_{0.9}$ (31) and $Pt_{0.5}Ni_{0.5}$ (30) indicate that as bulk Pt content decreases, so does the 2nd-layer Pt content, consistent with the trend predicted by the cluster expansion (Fig. 4C). The 2nd-layer composition for the record-setting Pt_3Ni catalyst is a Pt-rich outlier in this trend (Fig. 4C).

We consider the alternative possibility that near a composition of Pt_3Ni, a metastable disordered phase persists to low temperatures, and the surface reaches equilibrium with the underlying metastable phase. Such a situation would not be captured on the bulk phase diagram, which only shows stable states. To evaluate the structure and activity of the metastable material, we assume it gets kinetically trapped in its equilibrium state at 600 K and the configurational entropy is unchanged at lower temperatures. We then adjust the free energy at lower temperatures accordingly (*SI Appendix* Section 3). In this alternative scenario, the low-temperature composition profile no longer matches that of the record-setting catalyst (*SI Appendix* Fig. S8) and the region of high activity near a composition of Pt_3Ni at low temperatures disappears (*SI Appendix* Fig. S9A), further indicating that bulk atomic order is responsible for the experimental observations at this composition.

It is somewhat surprising to find the best agreement with experiment in the ordered region of the phase diagram, as Pt–Ni alloys are known to order slowly (32). There is no ordered Pt_3Ni region on many experimental Pt–Ni phase diagrams (32-34), despite theoretical predictions (20), which have since been experimentally confirmed (16, 17), that such a phase exists. Using the experimentally-determined expression for the order parameter relaxation time of PtNi at 735-800 K (32) as a rough approximation of kinetics of Pt_3Ni at lower temperatures, the relaxation time at 650 K would already be expected to on the order of several months. This suggests that it is unlikely that the system reached its equilibrium ordered state at a temperature of 400K on an experimental time scale. However annealing a Pt_3Ni crystal at a temperature of 613 K has shown the formation of small (~10 nm) ordered regions, with approximately 20% of the material reaching the ordered state in less than 10 hours (assuming the regions are fully ordered) (17, 35). Ordered regions were observed to form near dislocations, which help accommodate the strain that accompanies order and may allow greater atomic mobility. For a similar reason ordering may be expected to occur more readily near the surface.

The high activity in the ordered phase relative to the solid solution near a composition of Pt_3Ni is consistent with the predicted average oxygen binding energies (Fig. 5A). The highly active Pt-rich ordered Pt_3Ni phase binds oxygen more strongly than the Pt_3Ni solid solution due to its ability to accommodate significantly larger amounts of Pt in the second layer (Fig. 3B) (5). This is illustrative of one of the benefits of intermetallic phases in catalysis, particularly in materials that are capable of accommodating off-stoichiometric substitutional disorder. Although intermetallic phases typically exist in a narrow bulk composition range, they may be able to accommodate significant amounts of off-stoichiometry near the surface, largely decoupling the natural relationship between surface composition and lattice parameter that is found in solid

solutions. Intuitively, intermetallic surfaces can accommodate this off-stoichiometry because any excess of one of the components naturally segregates to the surface, where it is less disruptive to long-range order. This behavior can be understood more rigorously by considering that the first derivative of μ (the difference between the chemical potentials of Pt and Ni) with respect to x_{Pt} (the mole fraction of Pt) is given by the second derivative of the free energy per atom with respect to x_{Pt}. As the free energy curves for intermetallic phases have greater curvature than those for solid solutions (*SI Appendix* Fig. S10), the chemical potentials near the surface change more rapidly with respect to bulk composition for intermetallic phases than they do for solid solutions (Fig. 1B). In the case of Pt–Ni alloys, this change in chemical potential is primarily responsible for the change in 2nd-layer composition (Fig. 1B and Fig. 3B).

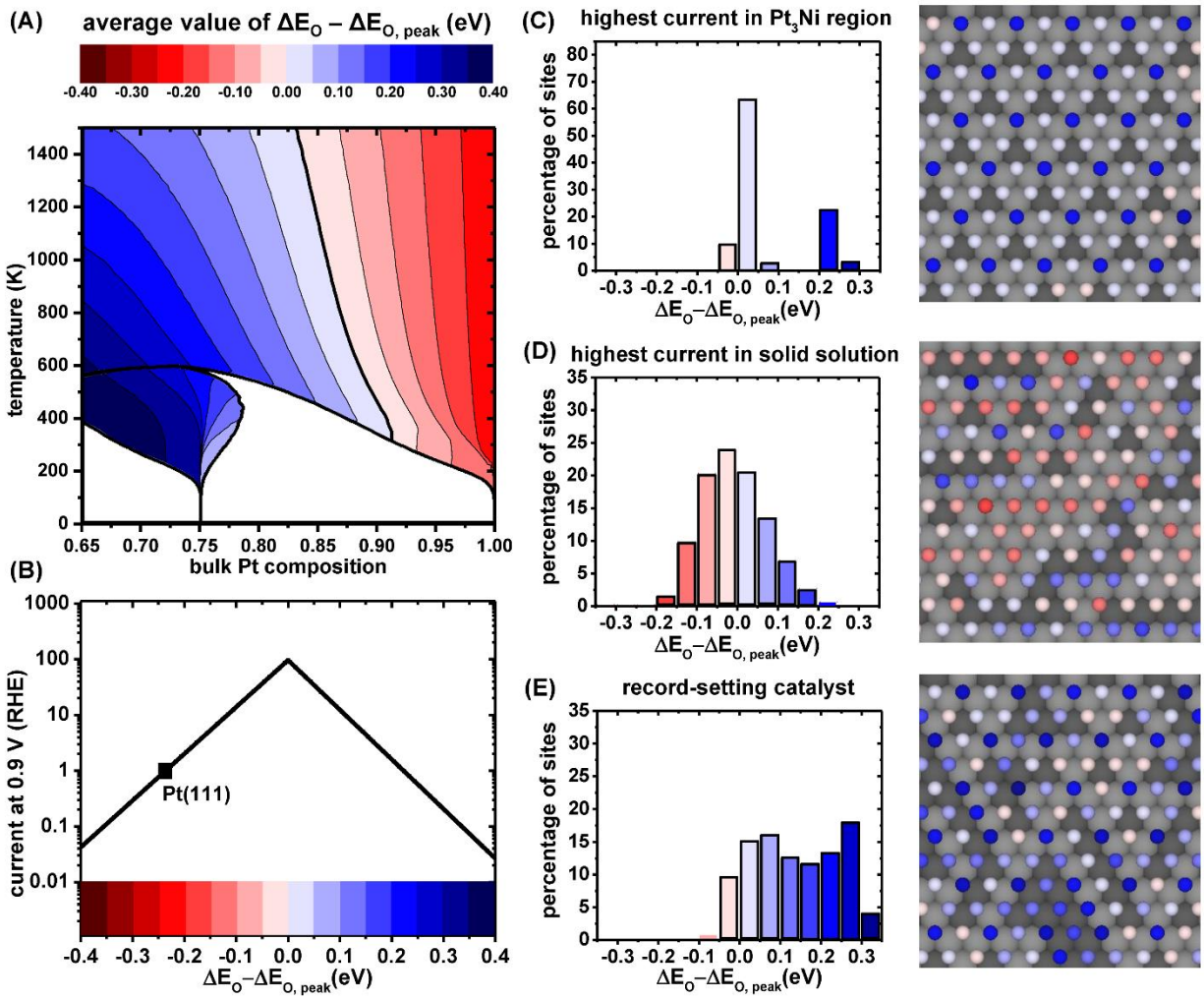

Fig. 5. Oxygen binding energies on Pt-Ni(111) surfaces. The oxygen binding energy, ΔE_O is defined in Eq. [6], and values are expressed relative to the peak of the volcano plot ($\Delta E_{O,\,peak}$). (A) The predicted average oxygen binding energy in equilibrium as a function of bulk Pt composition and temperature. The thick black line in figure A marks the peak of the volcano plot. (B) The Sabatier volcano plot relating ΔE_O to the current at 0.9 V vs. RHE, relative to Pt(111), at 298 K. (C-E) Histograms and surface snapshots showing the distribution of oxygen binding energies on (C) the surface with highest predicted specific activity, (D) the surface with the highest specific activity in the solid-solution region, and (E) the surface with a composition profile similar to the record-setting Pt_3Ni catalyst. The large medium grey and dark grey spheres represent Pt and Ni atoms, respectively. The second layer of Pt and Ni atoms are shown, as the first layer is pure Pt skin. The small spheres with the varied colors represent the oxygen atoms with binding energies given by the color bar in (B).

The average oxygen binding energy in the highly-active region in the solid solution phase is closer peak of the volcano plot (Fig. 5B) than the average oxygen binding energy in the highly-

active region in the ordered phase (Fig. 5A), but the peak activity in the ordered phase is predicted to be higher. This is due to the distribution of oxygen binding energies; in the ordered phase there is a higher density of sites with oxygen binding energies near the peak of the volcano plot (Fig. 5C). As the current depends exponentially on the oxygen binding energy (Fig. 5B), the average current is higher than the average oxygen binding energy would suggest (Fig. 2A and Fig. 5A). This exemplifies another benefit of intermetallic phases in catalysis, in that their underlying order can result in high concentrations of highly active sites. The point in the phase diagram that best corresponds to the composition profile of the record-setting catalyst has a disordered 2nd layer (Fig. 5E and Fig. S5A), similar to what we have predicted in previous work (5, 11). As a result, there is a greater spread in catalytic activities among its surface sites than there is in the more ordered surface (Fig. 5C and E), leading to lower catalytic activity. These results suggest that by synthesizing a fully ordered catalyst it is possible to achieve even greater catalytic activity in Pt_3Ni than what has already been achieved. However synthesizing the appropriate ordered state in a reasonable amount of time may be a significant challenge. This is particularly true for nanoparticles, as annealing them at elevated temperatures can result in particle aggregation (36). We note that ordered PtNi nanoparticles (37) and $L1_2$-ordered Pt_3Co nanoparticles (38-40) have been successfully synthesized, although the ordering in Pt_3Co likely occurs more readily than in Pt_3Ni (32).

There are regions in the Pt–Ni phase diagram in which there is a discontinuous change in the surface structure and composition with an incremental change in bulk composition (Fig. 3). These areas indicate surface phase transformations. It may be surprising to see a discontinuous change in structure with respect to bulk composition, as this does not happen with bulk phases; there is always a two-phase region that provides a transition between bulk phases as the bulk

composition is changed. However the surface phase is largely determined by the bulk chemical potentials, and it is possible for an incremental change in chemical potentials to result in a discontinuous phase transformation. This is particularly notable in the Pt_3Ni region, where a small decrease in the bulk composition below that of stoichiometric Pt_3Ni has a catastrophic effect on the predicted catalytic activity of the equilibrium surface structure (Fig. 2A). As the Pt composition decreases and the chemical potential of Ni increases relative to that of Pt, the surface becomes more Ni-rich and transforms from a phase with a Pt-rich 2nd layer (Fig. S3C) to a phase with nearly pure Ni in the 2nd layer (Fig. S3E), dramatically weakening the oxygen binding on the surface (Fig. 5A). Such surface phase transformations may be particularly important in systems in which ordering occurs more readily, such as Pt–Co (32).

We consider the sensitivity of our results to some of the assumptions inherent in our model. The shape of the volcano plot on the fcc(111) surface for the ORR has been well established both experimentally (41, 42) and theoretically (5, 9, 26). However the exact value of the peak of the volcano plot is not well defined, and there might be some errors in our calculated oxygen binding energies that shift the optimal calculated binding energy (43). If the peak of the volcano plot were shifted 25 meV to the right, decreasing the strength of oxygen binding at the peak, the regions of maximal catalytic activity in the activity map would shift to the left, towards more Ni-rich compositions (*SI Appendix* Fig. S11A). Similarly, if the peak of the volcano plot were shifted 25 meV to the left, the regions of maximal catalytic activity would shift to the right (*SI Appendix* Fig. S11B). Results similar to a leftward 25 meV shift in the peak are obtained if it is assumed that the bulk lattice parameter contracts by 0.25%, as might occur in a 5 nm nanoparticle (44) (*SI Appendix* Fig. S11C). These results are all consistent with known trends in oxygen binding energy with respect to composition and lattice parameter (5, 45, 46). In each of

these cases, the qualitative pattern in the activity map remains the same: there is a region of high catalytic activity on the Pt-rich side of the ordered Pt_3Ni phase, and another region of high catalytic activity for more Pt-rich compositions in solid solutions.

Conclusions

Surface structure and catalytic activity maps of alloy phase diagrams enable researchers to identify targets for synthesis and to gain insight into observed trends in catalytic activity. By creating such a map for the Pt-rich compositions of Pt–Ni alloys, we predict that optimal catalytic activity of a Pt–Ni solid solution occurs at a composition more Pt-rich than Pt_3Ni. We also show that the observed (111) surface composition profiles for Pt–Ni alloys are likely due to surfaces that became kinetically trapped at a temperature of about 600 K after annealing at higher temperatures. The record-setting Pt_3Ni catalyst is an outlier in this trend. The composition profile of the record-setting catalyst most closely matches that of an equilibrium surface of a slightly off-stoichiometric intermetallic Pt_3Ni phase, at a point in the phase diagram close to that which is predicted to have maximal catalytic activity. These data suggest that high catalytic activity on the $Pt_3Ni(111)$ surface is due to at least partial formation of ordered $L1_2$ domains, which can be achieved by annealing a Pt_3Ni alloy at a temperature of around 613 K. Such an approach may result in a highly stable and active catalyst, but the difficulty in achieving this state may explain why to date, no ORR catalyst has been reported to have higher specific activity than that reported by Stamenkovic et al. (11).

The surface structure and catalytic activity maps also clearly demonstrate some of the benefits of intermetallic phases for catalysis. Intermetallic phases that allow for substitutional disorder, such as Pt_3Ni, are able to accommodate large changes in surface composition with relatively

little change in lattice parameter, providing a way to largely decouple the near-surface composition from the lattice parameter (Fig. 2B), which may be useful for catalyst design. Catalytic activity can be further enhanced by achieving a state in which the near-surface layers have atomic order driven by the underlying bulk, which can result in a high density of catalytically active sites. However the formation of ordered surface phases also introduces surface phase transformations, in which an incremental change in bulk composition can have a large and discontinuous effect on the catalytic activity of the equilibrium surface structure.

Methodology

We implement our approach using the cluster expansion method (7, 47), which we have previously used to study the catalytic activity of the (111) surface of stoichiometric Pt_3Ni (5). In such a system, in which the lattice parameter of the surface is fixed, the total energy of the system can be expressed as:

$$E(\mathbf{s}) = V_0 + \sum_{\text{clusters}} V_{\text{cluster}} \prod_{i \in \text{cluster}} s_i, \qquad [1]$$

where $E(\mathbf{s})$ is the total energy as a function of the "site variables", s_i, used to represent the occupancy of each site. For a Pt–Ni slab with up to one monolayer of oxygen atoms adsorbed on the fcc sites, we use $s_i = 1$ for Ni or O and $s_i = -1$ for Pt or a vacancy (*SI Appendix* Fig. S1). The coefficients, V_{cluster}, are called effective cluster interactions (ECIs) and are typically fit to DFT calculations on structures with different atomic arrangements.

Eq. [1] cannot be used to model the surfaces of alloys for which the bulk lattice parameter is not fixed (e.g. alloys with varying composition). This is because the lattice parameter and energy of the slab will depend on the underlying bulk lattice parameter, but the bulk lattice parameter is

not a variable in Eq. [1]. We address this problem by explicitly expressing the ECI for each cluster as a quadratic equation of the lattice parameter a:

$$V_{\text{cluster}} = V_{\text{cluster},0} + V_{\text{cluster},1}a + V_{\text{cluster},2}a^2 \quad [2]$$

where $V_{\text{cluster},0}$, $V_{\text{cluster},1}$, $V_{\text{cluster},2}$ are three coefficients that we fit to DFT calculations. Eq. [2] assumes linear elasticity, which we believe is a reasonable approximation for many alloy surfaces and works well for the Pt–Ni system presented here. Eq. [2] also assumes that the variation in the underlying bulk lattice parameter in the directions parallel to the surface is isotropic, which is valid for the Pt-rich Pt–Ni(111) surfaces studied here. For systems in which the assumption of isotropic lattice parameters is not valid Eq. [2] can be generalized by introducing direction-dependent terms.

The ECIs of the cluster expansions were fit using the Bayesian method (48), which is particularly effective for nanoparticles and surfaces (5, 49). The determination of the regularization matrix, $\mathbf{\Lambda}$, for the slab cluster expansion is complicated by the fact that Eq. [2] contains three coefficients for each cluster orbit. As the units (and expected magnitudes) of these coefficients are all different, it is necessary to regularize each of these coefficients independently. We did this by first constructing a usual regularization matrix, $\mathbf{\Lambda_1}$, based on the number of sites in a cluster, the distance between sites, and cluster congruency (48). The full regularization matrix was then constructed as follows:

$$\mathbf{\Lambda} = \begin{bmatrix} \lambda_i\lambda_i\mathbf{\Lambda_1}, & \lambda_i\lambda_j\mathbf{\Lambda_1}, & \lambda_i\lambda_k\mathbf{\Lambda_1} \\ \lambda_i\lambda_j\mathbf{\Lambda_1}, & \lambda_j\lambda_j\mathbf{\Lambda_1}, & \lambda_j\lambda_k\mathbf{\Lambda_1} \\ \lambda_i\lambda_k\mathbf{\Lambda_1}, & \lambda_j\lambda_k\mathbf{\Lambda_1}, & \lambda_k\lambda_k\mathbf{\Lambda_1} \end{bmatrix} \quad [3]$$

where λ_i , λ_j and λ_k are three new regularization parameters introduced to account for the different expected magnitudes of $V_{\text{cluster},0}$, $V_{\text{cluster},1}$, and $V_{\text{cluster},2}$ in Eq. [2]. All regularization parameters were optimized simultaneously when fitting the cluster expansion.

To achieve thermodynamic equilibrium between the bulk and slab, their lattice parameters, temperatures, and chemical potentials must match. For a binary system such as Pt–Ni only the difference between the Pt and Ni chemical potentials matters, and we refer to this difference as

$$\mu \equiv \mu(\text{Pt}) - \mu(\text{Ni}) . \qquad [4]$$

For different values of the temperature and μ , we used a bulk Pt-Ni cluster expansion in grand canonical Monte Carlo simulations to determine the equilibrium composition of the bulk material. We then use Vegard's law (50) to estimate the equilibrium lattice parameter from the composition. Because we are interested in the Pt-rich region of the phase diagram, we used Pt_3Ni and Pt as reference states for Vegard's law:

$$a(x) = \frac{1-x}{0.25} a_{Pt_3Ni} + \frac{x-0.75}{0.25} a_{Pt} , \qquad [5]$$

where x is the bulk Pt composition, $a(x)$ is the lattice parameter of $Pt_xNi_{(1-x)}$ and a_{Pt_3Ni} and a_{Pt} are the DFT-calculated lattice parameters for Pt_3Ni and Pt, respectively. We found that this was a good approximation for the lattice parameters of different Pt–Ni bulk materials determined using DFT. With a lattice parameter matching that of the bulk material, the slab cluster expansion was then used to calculate the equilibrium structures and properties of the surface by running a grand canonical Monte Carlo simulation in which the chemical potentials and temperatures matched those used in the Monte Carlo simulation of the underlying bulk.

The bulk cluster expansion included 12 clusters and was trained on 157 structures. The leave-one-out cross validation (LOOCV) error, a measure of predictive accuracy relative to DFT (51),

was 3.5 meV per atom. For the slab cluster expansion, 205 clusters and 426 training structures were used, and the LOOCV error was 4.1 meV per atom. The Pt–Ni bulk phase diagram was generated using the Alloy Theory Automated Toolkit (ATAT) (51, 52).

We calculate the ORR current for a Pt–Ni(111) surface in a way similar to our previous work on Pt_3Ni (5). For each surface structure in the Metropolis Monte Carlo simulation, we used the slab cluster expansion to calculate oxygen binding energies (ΔE_O) at each site on the surface. Here ΔE_O was calculated as

$$\Delta E_O = E_{DFT}\left(slab + *O\right) - E_{DFT}\left(slab\right) + E_{DFT}\left(H_2\right) - E_{DFT}\left(H_2O\right) \quad [6]$$

where $E_{DFT}\left(slab + *O\right)$ is the total DFT energy of the slab with an adsorbed oxygen atom, $E_{DFT}\left(slab\right)$ is the DFT energy of the clean slab, and $E_{DFT}\left(H_2\right)$ and $E_{DFT}\left(H_2O\right)$ are the DFT energies of gas-phase H_2 and H_2O (5). In this convention, more negative values of ΔE_O indicate stronger oxygen binding. These oxygen binding energies were then used to calculate the current at each site through a Sabatier volcano, assuming the associative mechanism (9, 26), and the total current for a surface was calculated by averaging over all sites on the surface. To estimate surface coverage effects, we used kinetic Monte Carlo calculations in which adsorption and desorption rates as a function of ΔE_O were set to match the Sabatier volcano (*SI Appendix* section 2.6).

DFT calculations were run using the Vienna Ab Initio Simulation Package (VASP) (53) and the RPBE exchange-correlation functional (54). The Ni, Pt_pv_GW, H_GW, and O_GW PBE projector-augmented wave (PAW) (55) potentials provided with VASP were used. VASP was run with accurate precision with a plane wave cutoff energy of 434 eV. The Brillouin zone was sampled using grids generated by the *k*-point grid server (56) with a minimum distance of 46.5 Å between real space lattice points. Spin polarization was taken into account in the calculations and

the Methfessel–Paxton method (57) of order 2 was employed to determine electron occupancies with a smearing parameter of 0.2 eV. The convergence criteria for the electronic self-consistent iteration and the ionic relaxation loop were set to be 10^{-4} eV and 10^{-3} eV, respectively.

Additional details about the methods we used are provided in the SI Appendix.

ASSOCIATED CONTENT

Supplementary Information Description

Theoretical details of the bulk and slab cluster expansions, Metropolis and kinetic Monte Carlo simulations, atomic structures of representative surfaces, and simulations of metastable solid solutions are provided.

Author information

***Corresponding Author**

Email: tmueller@jhu.edu

Phone: (410) 516-5779

Author Contributions

L.C. and T.M. designed the research. L.C. and L.N. performed the research. L.C. and T.M. analyzed the data and wrote the manuscript. All authors have given approval to the final version of the manuscript.

Notes

The authors declare no competing financial interests.

Acknowledgments

We thank for Chao Wang, Yu Huang, and Zipeng Zhao for helpful discussion. This work was funded by the National Science Foundation under award DMR-1352373, using computational resources provided by XSEDE through awards DMR140068 and by the Maryland Advanced Research Computing Center (MARCC). Atomic-scale structural images were generated using VESTA (58).

References

1. Greeley J, Jaramillo TF, Bonde J, Chorkendorff I, & Nørskov JK (2006) Computational high-throughput screening of electrocatalytic materials for hydrogen evolution. *Nat. Mater.* 5:909.
2. Nørskov JK, Bligaard T, Rossmeisl J, & Christensen CH (2009) Towards the computational design of solid catalysts. *Nat. Chem.* 1:37.
3. Rostamikia G & Janik MJ (2010) Direct borohydride oxidation: mechanism determination and design of alloy catalysts guided by density functional theory. *Energy Environ. Sci.* 3(9):1262-1274.
4. Xin H, Holewinski A, & Linic S (2012) Predictive Structure–Reactivity Models for Rapid Screening of Pt-Based Multimetallic Electrocatalysts for the Oxygen Reduction Reaction. *ACS Catal.* 2(1):12-16.
5. Cao L & Mueller T (2015) Rational Design of Pt_3Ni Surface Structures for the Oxygen Reduction Reaction. *J. Phys. Chem. C* 119(31):17735-17747.
6. Calle-Vallejo F, *et al.* (2015) Finding optimal surface sites on heterogeneous catalysts by counting nearest neighbors. *Science* 350(6257):185.
7. Sanchez JM, Ducastelle F, & Gratias D (1984) Generalized Cluster Description of Multicomponent Systems. *Phys. A (Amsterdam, Neth.)* 128(1–2):334-350.
8. Kohn W & Sham LJ (1965) Self-Consistent Equations Including Exchange and Correlation Effects. *Phys. Rev.* 140(4A):A1133-A1138.
9. Norskov JK, *et al.* (2004) Origin of the Overpotential for Oxygen Reduction at a Fuel-Cell Cathode. *J. Phys. Chem. B* 108:17886-17892.

10. Zhao Z, *et al.* (2019) Pt-Based Nanocrystal for Electrocatalytic Oxygen Reduction. *Adv. Mater.* 0(0):1808115.
11. Stamenkovic VR, *et al.* (2007) Improved Oxygen Reduction Activity on $Pt_3Ni(111)$ via Increased Surface Site Availability. *Science* 315:493-497.
12. Sha Y, Yu TH, Merinov BV, Shirvanian P, & Goddard WA, III (2012) Mechanism for Oxygen Reduction Reaction on Pt3Ni Alloy Fuel Cell Cathode. *J. Phys. Chem. C* 116:21334-21342.
13. Matanovic I, Garzon FH, & Henson NJ (2011) Theoretical Study of Electrochemical Processes on Pt-Ni Alloys. *J. Phys. Chem. C* 115:10640-10650.
14. Yan Y, *et al.* (2017) Intermetallic Nanocrystals: Syntheses and Catalytic Applications. *Adv. Mater.* 29(14):1605997.
15. Gamler JTL, Ashberry HM, Skrabalak SE, & Koczkur KM (2018) Random Alloyed versus Intermetallic Nanoparticles: A Comparison of Electrocatalytic Performance. *Adv. Mater.* 30(40):1801563.
16. Schönfeld B, Engelke M, & Ruban AV (2009) Lack of support for adaptive superstructure $NiPt_7$: Experiment and first-principles calculations. *Phys. Rev. B* 79(6):064201.
17. Schönfeld B, Engelke M, & Sologubenko AS (2015) Microstructure and order in NiPt3. *Philosophical Magazine* 95(10):1080-1092.
18. Lu X-G, Sundman B, & A˚gren J (2009) Thermodynamic assessments of the Ni–Pt and Al–Ni–Pt systems. *Calphad* 33(3):450-456.
19. Sanati M, Wang LG, & Zunger A (2003) Adaptive Crystal Structures: CuAu and NiPt. *Phys. Rev. Lett.* 90(4):045502.
20. Dahmani CE, Cadeville MC, Sanchez JM, & Moran-Lopez JL (1985) Nickel-Platinum Phase Diagram: Experiment and Theory. *Phys. Rev. Lett.* 55(11):1208-1211.
21. Huang X, *et al.* (2015) High-Performance Transition Metal-doped Pt_3Ni Octahedra for Oxygen Reduction Reaction. *Science* 348(6240):1230-1234.
22. Cao L & Mueller T (2016) Theoretical Insights into the Effects of Oxidation and Mo-Doping on the Structure and Stability of Pt-Ni Nanoparticles *Nano Lett.* 16(12):7748-7754.
23. Jia Q, *et al.* (2018) Roles of Mo Surface Dopants in Enhancing the ORR Performance of Octahedral PtNi Nanoparticles. *Nano Lett.* 18(2):798-804.
24. Menning CA & Chen JG (2010) Regenerating Pt–3d–Pt model electrocatalysts through oxidation–reduction cycles monitored at atmospheric pressure. *Journal of Power Sources* 195(10):3140-3144.
25. Menning CA & Chen JG (2008) Thermodynamics and kinetics of oxygen-induced segregation of 3d metals in Pt–3d–Pt(111) and Pt–3d–Pt(100) bimetallic structures. *The Journal of Chemical Physics* 128(16):164703.
26. Karlberg GS, Rossmeisl J, & Norskov JK (2007) Estimations of Electric Field Effects on the Oxygen Reduction Reaction based on the Density Functional Theory. *Phys. Chem. Chem. Phys.* 9:5158-5161.
27. Nørskov JK, *et al.* (2008) The nature of the active site in heterogeneous metal catalysis. *Chem. Soc. Rev.* 37(10):2163-2171.
28. Qi L & Li J (2012) Adsorbate interactions on surface lead to a flattened Sabatier volcano plot in reduction of oxygen. *Journal of Catalysis* 295:59-69.

29. Bligaard T NJK, Dahl S, Matthiesen J, Christensen C H & J S (2004) The Brønsted-Evans-Polanyi relation and the volcano curve in heterogeneous catalysis. *J. Catal.* 224(1):206.
30. Gauthier Y, Joly Y, Baudoing R, & Rundgren J (1985) Surface-sandwich segregation on nondilute bimetallic alloys: $Pt_{50}Ni_{50}$ and $Pt_{78}Ni_{22}$ probed by low-energy electron diffraction. *Phys. Rev. B* 31(10):6216-6218.
31. Baudoing R, Gauthier Y, Lundberg M, & Rundgren J (1986) Surface segregation on Pt0.1Ni0.9(111) measured two layers deep by low-energy electron diffraction. *Journal of Physics C: Solid State Physics* 19(16):2825-2831.
32. Dahmani CE, Cadeville MC, & Pierron-Bohnes V (1985) Temperature dependences of atomic order relaxations in Ni-Pt and Co-Pt alloys. *Acta Metall.* 33(3):369-377.
33. Nash P & Singleton MF (1989) The Ni-Pt (Nickel-Platinum) system. *Bulletin of Alloy Phase Diagrams* 10(3):258-262.
34. Rakhtsaum G (2013) Platinum Alloys: A Selective Review of the Available Literature. *Platinum Metals Review* 57(3):202-213.
35. Schönfeld B, Engelke M, & Ruban AV (2011) Order and Disorder in Ni-Pt Single Crystals. *Solid State Phenomena* 172-174:593-601.
36. Li J, *et al.* (2019) Facile and Large-Scale Fabrication of Sub-3 nm PtNi Nanoparticles Supported on Porous Carbon Sheet: A Bifunctional Material for the Hydrogen Evolution Reaction and Hydrogenation. *Chem. - Eur. J.* 25(29):7191-7200.
37. Leonard BM, Zhou Q, Wu D, & DiSalvo FJ (2011) Facile Synthesis of PtNi Intermetallic Nanoparticles: Influence of Reducing Agent and Precursors on Electrocatalytic Activity. *Chem. Mater.* 23(5):1136-1146.
38. Wang D, *et al.* (2012) Structurally ordered intermetallic platinum–cobalt core–shell nanoparticles with enhanced activity and stability as oxygen reduction electrocatalysts. *Nat. Mater.* 12:81.
39. Xiong Y, *et al.* (2019) Revealing the atomic ordering of binary intermetallics using in situ heating techniques at multilength scales. *Proc. Natl. Acad. Sci. U. S. A.* 116(6):1974.
40. Chi M, *et al.* (2015) Surface faceting and elemental diffusion behaviour at atomic scale for alloy nanoparticles during in situ annealing. *Nat. Commun.* 6:8925.
41. Stamenkovic V, *et al.* (2006) Changing the Activity of Electrocatalysts for Oxygen Reduction by Tuning the Surface Electronic Structure. *Angew. Chem., Int. Ed.* 45:2897-2901.
42. Greeley J, *et al.* (2009) Alloys of Platinum and Early Transition Metals as Oxygen Reduction Electrocatalysts. *Nat. Chem.* 1:552-556.
43. Deshpande S, Kitchin JR, & Viswanathan V (2016) Quantifying Uncertainty in Activity Volcano Relationships for Oxygen Reduction Reaction. *ACS Catal.* 6(8):5251-5259.
44. Leontyev IN, *et al.* (2014) Size dependence of the lattice parameters of carbon supported platinum nanoparticles: X-ray diffraction analysis and theoretical considerations. *RSC Adv.* 4(68):35959-35965.
45. Hyman MP & Medlin JW (2007) Effects of Electronic Structure Modifications on the Adsorption of Oxygen Reduction Reaction Intermediates on Model Pt(111)-Alloy Surfaces. *J. Phys. Chem. C* 111:17052-17060.
46. Xu W, Cheng D, Niu M, Shao X, & Wang W (2012) Modification of the Adsorption Properties of O and OH on Pt-Ni Bimetallic Surfaces by Subsurface Alloying. *Electrochim. Acta* 76:440-445.

47. Cao L, Li C, & Mueller T (2018) The Use of Cluster Expansions To Predict the Structures and Properties of Surfaces and Nanostructured Materials. *Journal of Chemical Information and Modeling* 58(12):2401-2413.
48. Mueller T & Ceder G (2009) Bayesian Approach to Cluster Expansions. *Phys. Rev. B* 80:024103.
49. Mueller T (2012) Ab initio Determination of Structure-Property Relationships in Alloy Nanoparticles. *Phys. Rev. B* 86:144201.
50. Vegard L (1921) Die Konstitution der Mischkristalle und die Raumfüllung der Atome. *Eur. Phys. J. A* 5(1):17-26.
51. Van de Walle A & Ceder G (2002) Automating First-Principles Phase Diagram Calculations. *J. Phase Equilib.* 23:348-359.
52. van de Walle A, Asta M, & Ceder G (2002) The alloy theoretic automated toolkit: A user guide. *CALPHAD* 26(4):539-553.
53. Kresse G & Furthmueller J (1996) Efficient Iterative Schemes for Ab initio Total-Energy Calculations Using a Plane-Wave Basis Set. *Phys. Rev. B* 54:11169-11186.
54. Hammer B, Hansen LB, & Nørskov JK (1999) Improved adsorption energetics within density-functional theory using revised Perdew-Burke-Ernzerhof functionals. *Physical Review B* 59(11):7413.
55. Blochl PE (1994) Projector Augmented-Wave Method. *Physical Review B* 50(24):17953-17979.
56. Wisesa P, McGill KA, & Mueller T (2016) Efficient Generation of Generalized Monkhorst-Pack Grids through the Use of Informatics. *Phys. Rev. B* 93(15):155109.
57. Methfessel M & Paxton AT (1989) High-Precision Sampling for Brillouin-Zone Integration in Metals. *Phys. Rev. B* 40(6):3616-3621.
58. Momma K & Izumi F (2008) VESTA: A Three-Dimensional Visualization System for Electronic and Structural Analysis. *J. Appl. Crystallogr.* 41:653-658.

Supplementary Information for

Computationally generated maps of surface structures and catalytic activities for alloy phase diagrams

Liang Cao[a], Le Niu[a], and Tim Mueller[a,*]

[a]Department of Materials Science and Engineering, Johns Hopkins University, Baltimore, MD 21218, USA

*Corresponding Author

Tim Mueller

Email: tmueller@jhu.edu

This PDF file includes:

Supplementary text

Figs. S1 to S11

Tables S1 to S3

References for SI

1. Simulations on bulk Pt–Ni

1.1 A Cluster expansion for bulk fcc Pt–Ni systems

The training set used to fit the bulk Pt–Ni cluster expansion consisted of an initial set of 130 random structures selected to sample configuration space in a way to minimize the variance in the predicted property values, as described by Mueller et al. (1, 2). As we mainly focus on the Pt-rich Pt–Ni catalysts, the Pt compositions of these structures were randomly sampled from a uniform distribution between 45% and 100%. The remaining structures were added every time the energy of a structure, such as ordered Pt_3Ni, was calculated with DFT. To reduce the prediction error of the cluster expansion, the two pure elements (Ni and Pt) and two ground-state structures (ordered PtNi and Pt_3Ni) were included twice in the training set (2), resulting in 157 total structures in the training set. The effective cluster interactions (ECIs) of the cluster expansion were fit to the DFT-calculated formation energies of fully relaxed structures relative to the reference states of bulk fcc Ni and Pt. Positions of Pt & Ni atoms and shapes & volumes of unit cells were relaxed. The DFT-calculated lattice parameters of bulk pure Ni, ordered PtNi, Pt_3Ni, and pure Pt are 3.553, 3.809, 3.906, and 3.996 Å, respectively.

The cluster expansion included the empty cluster, the one-body (point) cluster, and all 2-body clusters up to the 9th-nearest neighbor, for a total of 12 symmetrically distinct cluster functions. The ECIs for these cluster functions were fit to the training data using the Bayesian approach (1) with a multivariate Gaussian prior distribution. The inverse of the covariance matrix for the prior distribution, Λ, had elements given by

$$\lambda_{\alpha\alpha} = \begin{cases} 0 & \text{for } n_\alpha = 0 \\ \lambda_1 & \text{for } n_\alpha = 1 \\ \lambda_2 e^{\lambda_3 r_\alpha} e^{\lambda_4 n_\alpha} & \text{for } n_\alpha > 1 \end{cases} \qquad [1]$$

where n_α is the number of sites in cluster function α, r_α is the maximum distance between sites, and the parameters λ_1, λ_2, λ_3, and λ_4 were determined by using a conjugate gradient algorithm to minimize the leave-one-out cross validation (LOO CV) score, an estimate of prediction error (3). The final values for these parameters were 2.484, 0.958, 0.020, and 0.078, respectively. The resulting cluster expansion had a root mean square LOO CV error of 3.5 meV per atom referenced to DFT calculations.

1.2 Generation of bulk Pt–Ni phase diagram

The equilibrium structures of bulk Pt–Ni were determined by Monte Carlo simulations in a grand canonical ensemble as a function of temperature and μ. The bulk elemental fcc structures at 0 K were chosen as reference states, so that the chemical potential of Pt in bulk fcc Pt is zero, and the chemical potential of Ni in bulk fcc Ni is zero. As we are interested in the Pt-rich Pt–Ni catalysts in this work, we identified the range of μ where the mole fractions of Pt in equilibrium structures are greater than or equal to 50%. Monte Carlo simulations based on bulk cluster expansion were run on a grand canonical ensemble to determine the range of μ mentioned above. All simulations on a grand canonical ensemble of bulk Pt–Ni in this work were run on super cells with the size of 16 × 16 × 16 primitive cells, temperature between zero and 1500 K with an increment of 20 K, and μ between 0.09 eV and 0.9 eV with an increment of 0.01 eV unless otherwise noted. For each combination of μ and temperature, the number of equilibration steps and recording steps for Monte Caro simulations are 1,296,000 and 3,888,000, respectively. The windows of μ in which bulk PtNi, Pt_3Ni, and pure Pt are stable at zero temperature (Table S1) are similar to DFT calculations and our previous work (4). The bulk phase diagram (Fig. 1) was calculated by running Monte Carlo simulations using the phb command from Alloy-Theoretic Automated Toolkit (ATAT) (3, 5-7). To be consistent with our own Monte Carlo simulations on bulk Pt–Ni, the unit cells used at ATAT were also 16 × 16 × 16.

Table S1. The DFT-calculated and cluster-expansion-predicted (CE-predicted) windows of μ (chemical potential difference between Pt and Ni) for bulk Pt–Ni alloys at 0 K.

pair structures of bulk Pt–Ni alloys in equilibrium	DFT-calculated μ / eV		CE-predicted μ / eV	
	minimum	maximum	minimum	maximum
PtNi	NA	0.090	NA	0.098
Pt_3Ni	0.090	0.287	0.098	0.288
pure Pt	0.287	∞	0.288	∞

2. Simulations on Pt–Ni slabs

2.1 A lattice-parameter-dependent cluster expansion for a 7-layer Pt–Ni(111) slab

The process of generating training data for the lattice-parameter-dependent cluster expansion on a 7-layer Pt–Ni(111) slab (Fig. S1, Fig. S2) is summarized as follows. The training set consisted of an initial set of 240 random structures, including 130 without adsorbed atomic oxygen and 110 with a random adsorbed oxygen coverage between zero and 1 monolayer (ML) selected to sample configuration space in a way to minimize the variance in the predicted property values, as described by Mueller et al. (1, 2). As the DFT-calculated lattice parameters for bulk ordered PtNi, Pt_3Ni and pure Pt are 3.809 Å, 3.906 Å and 3.996 Å, respectively, the lattice parameters of these training structures were randomly sampled from an uniform distribution between 3.672 Å and 4.140 Å to cover the lower (upper) bound of 3.809 Å (3.996 Å) for bulk PtNi (pure Pt). The remaining structures were added every time the energy of a different structure, such as a predicted ground-state structure, was calculated with DFT, resulting in 426 total structures in the training set.

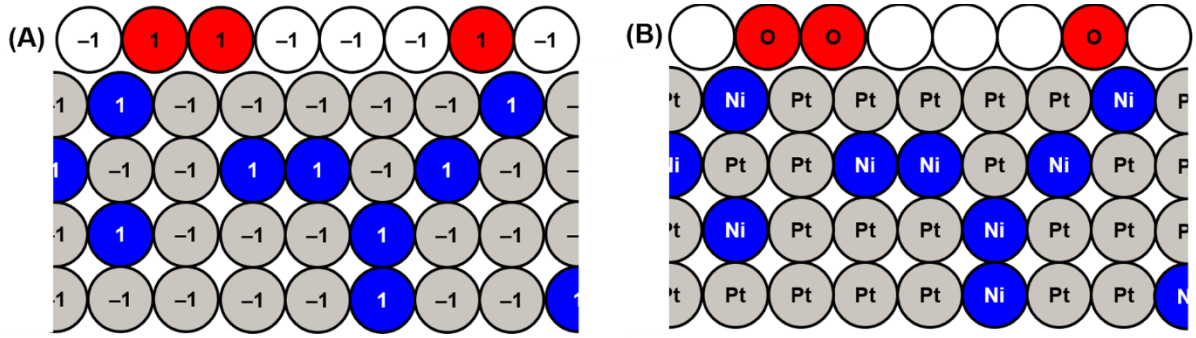

Fig. S1. A schematic illustration of a slab model in a binary cluster expansion with adsorbates. (A) How site variables are assigned for (B) an example of surface structure. In figure A, Ni and O atoms are marked as "1", Pt and vacancy atoms are marked as "−1". Grey, blue, red, and white spheres represent the Pt, Ni, O, and vacancy atoms, respectively.

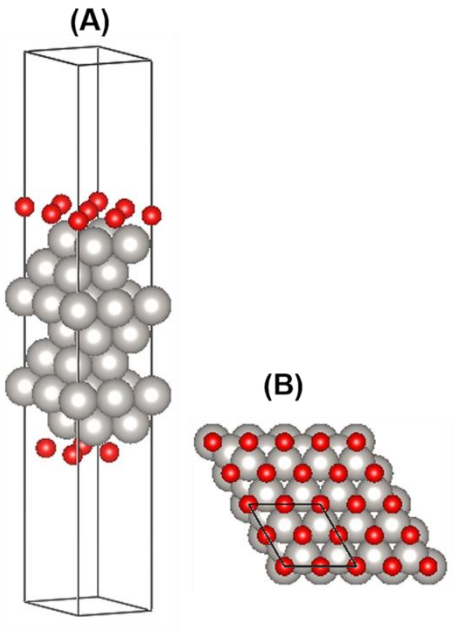

Fig. S2. The 7-layer Pt–Ni(111) slab model with a monolayer of adsorbed atomic oxygen used for slab cluster expansion. (A) The side view of a 2 × 2 (111) unit cell and (B) top view of a 4 × 4 (111) unit cell. In figures A and B, Grey spheres can be occupied by Pt or Ni, and the red spheres in fcc hollow sites on the surface could be occupied by oxygen or vacancy.

The lattice-parameter-dependent cluster expansion included the empty cluster, the one-body (point) cluster, all 2-body clusters up to the 31st-nearest neighbor, all 3-body clusters up to the third-nearest neighbor, and all 4-body clusters up to the third-nearest neighbor, for a total of 196 symmetrically distinct clusters. To accurately account for the interactions between oxygen atoms on the Pt–Ni(111) surfaces with relatively high coverages of adsorbed oxygen, the cutoff distances for 3-body clusters and 4-body clusters that only contain oxygen/vacancy sites were increased to include 3-body clusters up to the fifth-nearest neighbor and 4-body clusters up to the fourth-nearest neighbor. This leads to a total of 205 symmetrically distinct clusters. According to Eq. [2] in the main body, there are 3 × 205 = 615 ECIs that needed to be fit. The ECIs for these cluster functions were fit to the training data (DFT-calculated formation energies) using the Bayesian approach (1) with a multivariate Gaussian prior distribution. The inverse of the covariance matrix for the prior distribution, Λ, had elements given by

$$\lambda_{\alpha\alpha} = \begin{cases} 0 & \text{for } \mathrm{n}_\alpha = 0 \\ e^{-\lambda_1} & \text{for } \mathrm{n}_\alpha = 1 \\ e^{-\lambda_2} e^{\lambda_3 r_\alpha} n_\alpha{}^{\lambda_4} & \text{for } \mathrm{n}_\alpha > 1 \end{cases} \qquad [2]$$

$$\lambda_{\alpha\beta} = \begin{cases} 0 & \text{if } \alpha \text{ and } \beta \text{ are not congruent} \\ \lambda_5 \lambda_{\alpha\alpha} & \text{if } \alpha \text{ and } \beta \text{ are congruent,} \end{cases}$$

where n_α is the number of sites in cluster function α, and r_α is the maximum distance between sites in Angstroms. To account for the different expected magnitudes of three coefficients in the quadratic equation for each cluster in Eq. [2] in the main body, we introduced three more parameters: λ_6, λ_7, and λ_8, which were used to construct a global regularization matrix as follows:

$$\mathbf{\Lambda} = \begin{bmatrix} \lambda_6\lambda_6\mathbf{\Lambda_1}, & \lambda_6\lambda_7\mathbf{\Lambda_1}, & \lambda_6\lambda_8\mathbf{\Lambda_1} \\ \lambda_6\lambda_7\mathbf{\Lambda_1}, & \lambda_7\lambda_7\mathbf{\Lambda_1}, & \lambda_7\lambda_8\mathbf{\Lambda_1} \\ \lambda_6\lambda_8\mathbf{\Lambda_1}, & \lambda_7\lambda_8\mathbf{\Lambda_1}, & \lambda_8\lambda_8\mathbf{\Lambda_1} \end{bmatrix} \qquad [3]$$

where the elements of $\mathbf{\Lambda_1}$ are defined in Eq. [2]. The parameters λ_1, λ_2, λ_3, λ_4, λ_5, λ_6, λ_7, and λ_8 were determined by using a conjugate gradient algorithm to minimize the leave-one-out cross validation (LOO CV) score, an estimate of prediction error (3). The final values for these parameters were 15.075, 15.407, 2.566, 1.702, 23.428, 0.798, 1.048, and 0.764, respectively. The resulting cluster expansion, used to predict energies through Eq. [1] and Eq. [2] in the main body, had a root mean square LOO CV error of 4.1 meV per atom referenced to DFT calculations.

2.2 Ground state slabs predicted by lattice-parameter-dependent cluster expansion

To mimic the underlying bulk Pt–Ni phase, the atomic orders of the 5th, 6th, and 7th layers of 7-layer slabs were randomly initialized using the following treatment.

(1) In the solid solution region of the bulk phase diagram (Fig. 1), the 5th, 6th, and 7th layers were initialized by randomly decorating with the bulk composition at that temperature.
(2) In the ordered Pt_3Ni region, the 5th, 6th, and 7th layers started with the ordered Pt_3Ni structure. For bulk Pt composition x>0.75, Ni atoms were randomly flipped to Pt atoms with probability $\frac{(x-0.75)}{0.25}$. For bulk Pt composition x<0.75, Pt atoms were randomly flipped to Ni atoms with probability $\frac{(0.75-x)}{0.75}$.

This treatment has been applied to all Monte Carlo simulations on Pt–Ni slabs unless otherwise noted, which makes sure that the 5-7 layers of slabs have the same bulk phase and Pt composition as the underlying bulk Pt–Ni materials.

In the two μ windows of stable bulk Pt_3Ni and pure Pt at 0 K (Table S1), we used Monte Carlo simulations on a grand canonical ensemble to identify the ground state near-surface structures. We found by using 2 × 2, 4 × 4, 8 × 8, and 12 × 12 unit cells on the Pt–Ni(111) surfaces, the identified ground state slabs at 0K could be reduced a 2 × 2 or 3 × 3 unit cell (Fig. S3). The μ windows of these ground state slabs are provided in Table S2, where the value of μ between each pair of two slabs with adjacent compositions was calculated as in our previous work (4). For the three ground state structures in equilibrium with bulk Pt_3Ni, the atomic structures of the top four layers for two of the slabs, which we label as $Pt_{22}Ni_6$ (Fig. S3C) and $Pt_{20}Ni_8$ (Fig. S3E), exactly match our previous results using a slab cluster expansion with a fixed lattice parameter (4). The third slab, which we label $Pt_{21}Ni_7$ (Fig. S3D), has 25% and 100% Pt in the 2nd and 3rd layers, respectively. This is different from the previously identified surface, which had 50% Pt and 75% Pt in the 2nd and 3rd layers, respectively (4). For the purpose of comparison, we label the surface with 50% and 75% Pt in the 2nd and 3rd layers as $Pt_{21}Ni_7$-new. The DFT-calculated (CE-predicted) energy of $Pt_{21}Ni_7$ is only 1.3 meV (1.0 meV) per atom lower than that of $Pt_{21}Ni_7$-new. The possible reasons for the difference with our previous results include the differences of slab thickness (7 layers in

this work and 9 layers in previous work (4)) and the parameters used in DFT calculations (e.g., the plane wave cutoff energy and the level of calculation precision in VASP).

Table S2. Windows of cluster-expansion-predicted μ for Pt–Ni ground state slabs at 0 K.

equilibrium bulk	μ / eV		equilibrium slab	μ / eV	
	minimum	maximum		minimum	maximum
Pt_3Ni	0.098	0.288	$Pt_{20}Ni_8$	0.098	0.234
			$Pt_{21}Ni_7$	0.234	0.251
			$Pt_{22}Ni_6$	0.251	0.288
Pt	0.288	∞	$Pt_{26}Ni_2$	0.288	0.353
			$Pt_{62}Ni_1$	0.353	0.375
			Pt_{28}	0.375	∞

Note: only the $Pt_{62}Ni_1$ slab is on a 3 × 3 unit cell, and all the other slabs are on a 2 × 2 unit cell.

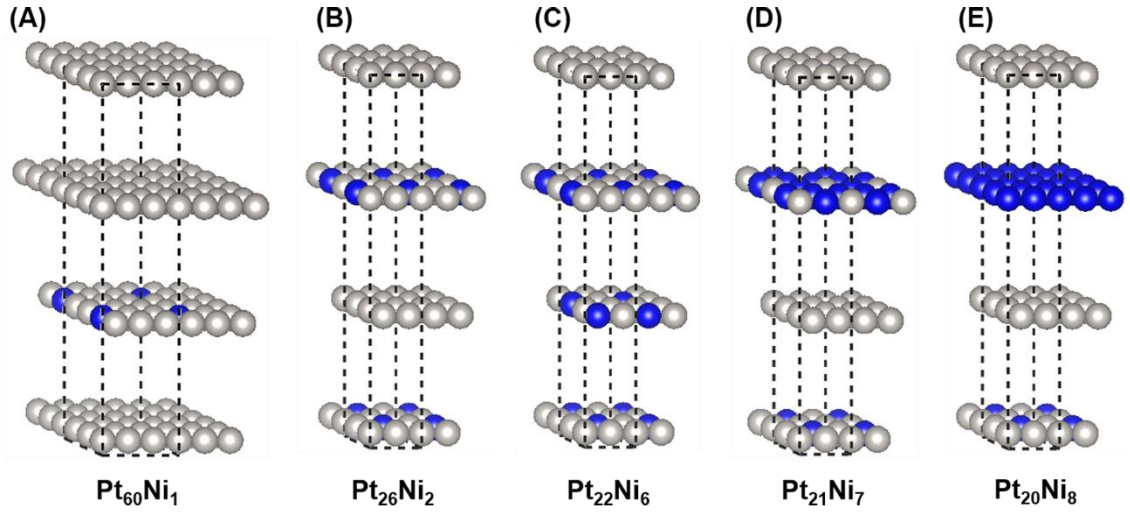

Fig. S3. The top four layers of (A, B) two ground state surfaces in equilibrium with bulk Pt and (C-E) three ground state surfaces in equilibrium with bulk Pt_3Ni at 0 K predicted using the same way in our previous work (4). A and B have the lattice parameter of Pt and C-E have the lattice parameter of Pt_3Ni. A and B have a pure Pt structure and C-E have an ordered Pt_3Ni structure in 5-7 layers. The grey and blue spheres are Pt and Ni atoms.

2.3 Ni surface segregation in oxidizing conditions

Our calculations indicate that at nearly all points of the Pt–Ni phase diagram considered in this study, exposure to 0.21 atm O_2 will drive segregation of Ni to the surface, where it will be oxidized and may dissolve. In the limit of dilute Ni in Pt, we calculate Ni will segregate to the surface at values of μ up to 1.31 eV. Nearly all points on the calculated phase diagram (Fig. 1B) have a chemical potential below this value. The segregation of Ni to the surface upon exposure to O_2 was further confirmed through Metropolis Monte Carlo simulations.

2.4 Calculation of the ORR current

In this work, we assume that the ORR happens through the associative mechanism based on previous studies (8, 9). The oxygen binding energy (ΔE_O, as defined in Eq. [6] in the main body) is related to the activation free energy, E_a, at an applied potential of 0.9 V (vs. the reversible hydrogen electrode, RHE) through a volcano plot (4, 8):

$$E_a = -\min(-0.297 + 0.5(\Delta E_O - 1.699), -0.297 + 0.53(1.699 - \Delta E_O)). \quad [4]$$

where all energies are given in eV. The peak position ($\Delta E_{O,\,peak}$=1.699 eV) of the volcano plot was determined by adding 0.236 eV to the oxygen binding energy on the surface of a 7-layer Pt(111) slab (ΔE_O=1.463 eV) with a 1/4 ML oxygen coverage. The oxygen binding energies used in Eq. [4] are at a 1/4 ML coverage of adsorbed oxygen unless otherwise noted. Each CE-predicted oxygen binding energy (ΔE_O) at 1/144 ML is converted to that at a 1/4 ML by adding a lattice-parameter-dependent lateral interaction energy. These interaction energies were calculated by taking the difference between ΔE_O on the $Pt_{22}Ni_6$ surface of a 2 × 2 (111) unit cell (Fig. S3C) at 1/4 ML coverage and ΔE_O on the same surface of a 12 × 12 (111) unit cell at 1/144 ML coverage as predicted by the lattice-parameter-dependent cluster expansion. The predicted ORR current (I_j) for a surface oxygen binding site *j* was then calculated using

$$I_j = I_0 \exp\left(\frac{-E_a}{kT}\right), \quad [5]$$

where I_0 is a constant, k is Boltzmann's constant, and T is the temperature in degrees Kelvin. The calculated ORR current relative to Pt(111) at 298 K as a function of $\Delta E_O - \Delta E_{O,\,peak}$ is shown in Fig. 5B in the main body. The predicted ORR current for a Pt–Ni(111) surface was then calculated as the average current over all oxygen binding sites:

$$\langle I \rangle = \frac{\sum_{j=1}^{N} I_j}{N} \; . \quad [6]$$

where I_j is the current at the jth site and the sum is over all binding sites in the unit cell. In this work, the predicted ORR current of a Pt–Ni surface is expressed relative to that of pure Pt(111) surface unless otherwise noted.

The cluster-expansion-predicted and DFT-calculated oxygen binding energies and ORR currents of several representative structures are in good agreement (Table S3), indicating the high level of accuracy of our lattice-parameter-dependent cluster expansion.

Table S3. A list of cluster-expansion-predicted and DFT-calculated oxygen binding energies (ΔE_O) and ORR currents on various Pt–Ni surfaces with varied lattice parameters. The values of ΔE_O and ORR current are referenced to those of pure Pt(111) surface in this work unless otherwise noted. CE stands for cluster expansion.

surface	applied lattice parameter (Å)	ΔE_O on strongest binding site (eV)		average ΔE_O (eV)		average current <*I*>	
		DFT	CE	DFT	CE	DFT	CE
ideal surface	NA	1.669		1.669		96.0	
pure Pt	3.996	0	–0.007	0	–0.007	1.0	0.88
	3.871	0.234	0.281	0.234	0.281	92.10	37.93
$Pt_{26}Ni_2$	3.996	–0.02	0.01	0.069	0.088	3.91	5.64
$Pt_{22}Ni_6$	3.913	0.241	0.228	0.308	0.289	65.12	61.92
	3.906	0.255	0.244	0.322	0.305	48.55	61.04
	3.885	0.293	0.292	0.362	0.351	22.18	22.99
$Pt_{21}Ni_7$	3.906	0.204	0.263	0.490	0.473	13.07	13.95
$Pt_{21}Ni_7$-new	3.906	0.269	0.264	0.414	0.396	24.31	26.97
	3.885	0.301	0.312	0.450	0.441	12.57	10.08
$Pt_{20}Ni_8$	3.906	0.587	0.564	0.590	0.564	0.07	0.12
	3.871	0.651	0.617	0.662	0.632	0.02	0.03
$Pt_{20}Ni_8$-new	3.885	0.323	0.333	0.548	0.530	4.07	3.34
$Pt_{20}Ni_8$-new-2	3.854	0.353	0.368	0.361	0.368	8.67	6.41
	3.906	0.264	0.250	0.266	0.251	54.02	71.22

Note: The layer-by-layer Pt compositions in the first, second, third, and fourth layers of "$Pt_{21}Ni_7$-new" surface are 100%, 50%, 75%, and 75% Pt, respectively; those of "$Pt_{20}Ni_8$-new" surface are 100%, 25%, 75%, and 75% Pt, respectively; and those of "$Pt_{20}Ni_8$-new-2" surface are 100%, 100%, 0%, and 75% Pt, respectively. The 5-7 layers of these three new surfaces are ordered Pt_3Ni.

2.5 Generation of the catalytic activity maps and surface composition profiles on Pt–Ni surfaces

To calculate the catalytic activity map of ORR current expressed in Eq. [6], we ran Monte Carlo simulations in a grand canonical ensemble on 7-layer Pt–Ni(111) slabs with lattice parameter determined by the underlying equilibrium bulk materials under the constraint that the bulk and slab had to be in thermodynamic equilibrium, with matching temperatures and chemical potentials. We used 12 × 12 (111) unit cells with 1008 Pt/Ni atoms and 144 O/Vacancy sites for all simulations on the extended surfaces unless otherwise noted. Each time a new structure was sampled in a Monte Carlo simulation, we calculated ΔE_O for a single oxygen atom on each fcc site (1/144 ML coverage) using the lattice-parameter-dependent cluster expansion. To convert the ΔE_O at 1/144 MLto 1/4 ML, a lattice-parameter-dependent lateral interaction energy as calculated in the previous subsection was added to the ΔE_O value at 1/144 ML coverage. Then we calculated the ORR current for each site and averaged over all 144 fcc sites to obtain the average ORR current for each new structure. We calculated the average surface composition profiles and catalytic activity maps in Fig. 2 and Fig. 3 of the main body by screening through μ from 0.09 eV to 0.9 eV with an increment of 0.01 eV (outer loop) and temperature from 0 K to 1500 K with an increment of 20 K (inner loop). The values of predicted ORR currents and composition profiles discussed in this work are averages over 10 independent parallel runs unless otherwise noted. For each combination of chemical potential and temperature during each parallel run, the parameters for Monte Caro simulation are: the number of equilibration steps is 1,296,000, the number of recording steps is 3,888,000. The 1^{st}, 2^{nd}, 3^{rd}, and 4^{th} layers of the initial slab structure for Monte Carlo simulation at each temperature was initialized from the last accepted structure from previous temperature, and the 5^{th}, 6^{th}, and 7^{th} layers were initialized according to the treatment described in section 2.2 of this document.

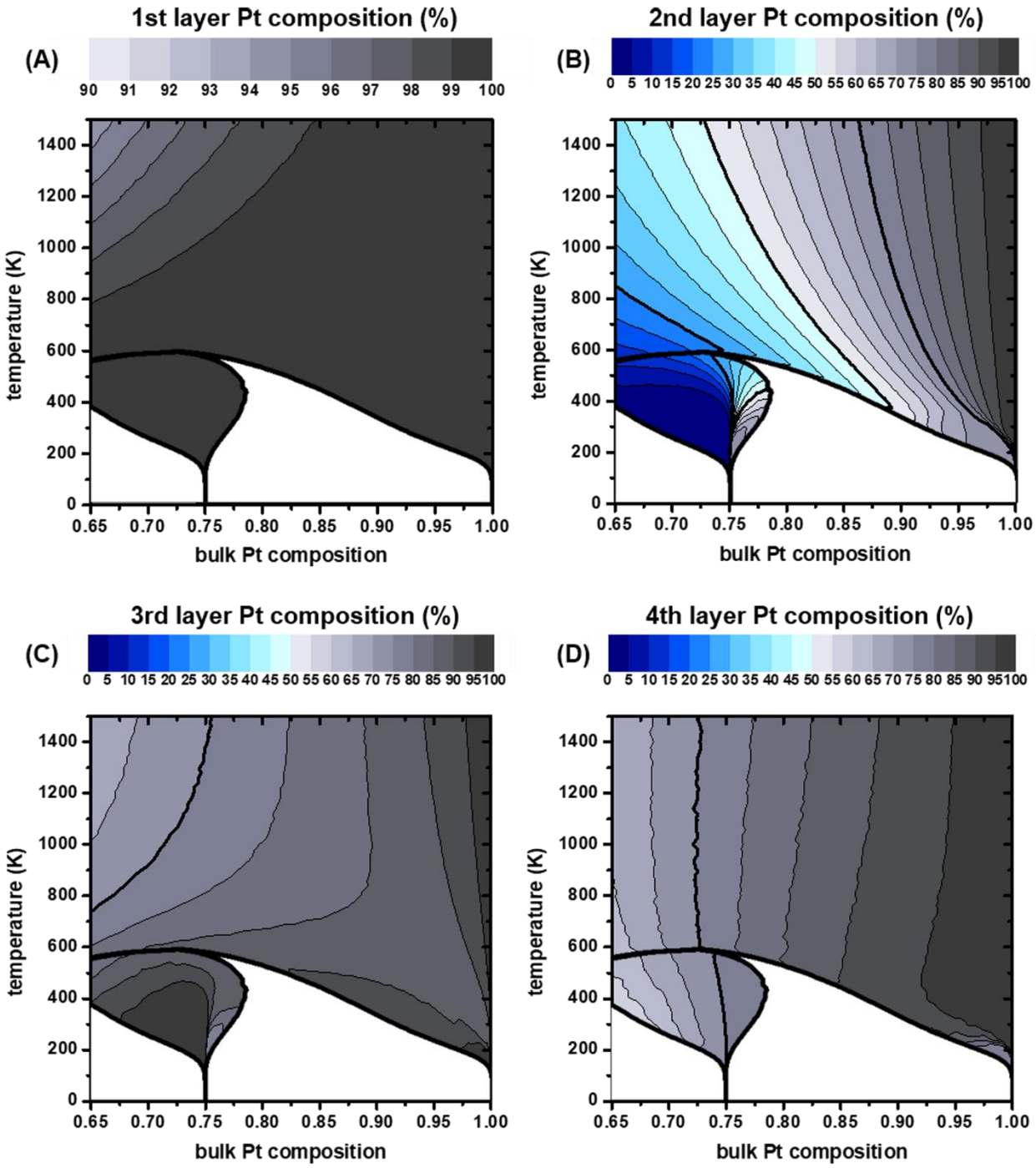

Fig. S4. Layer-by-layer composition maps on slabs. The predicted Pt compositions in the (A) first, (B) second, (D) third, and (D) fourth layers of Pt–Ni(111) surfaces as a function of bulk Pt composition and temperature. Thick black lines mark Pt compositions that are multiples of 0.25. Figures (A) and (B) are shown in Fig. 3 in the main text.

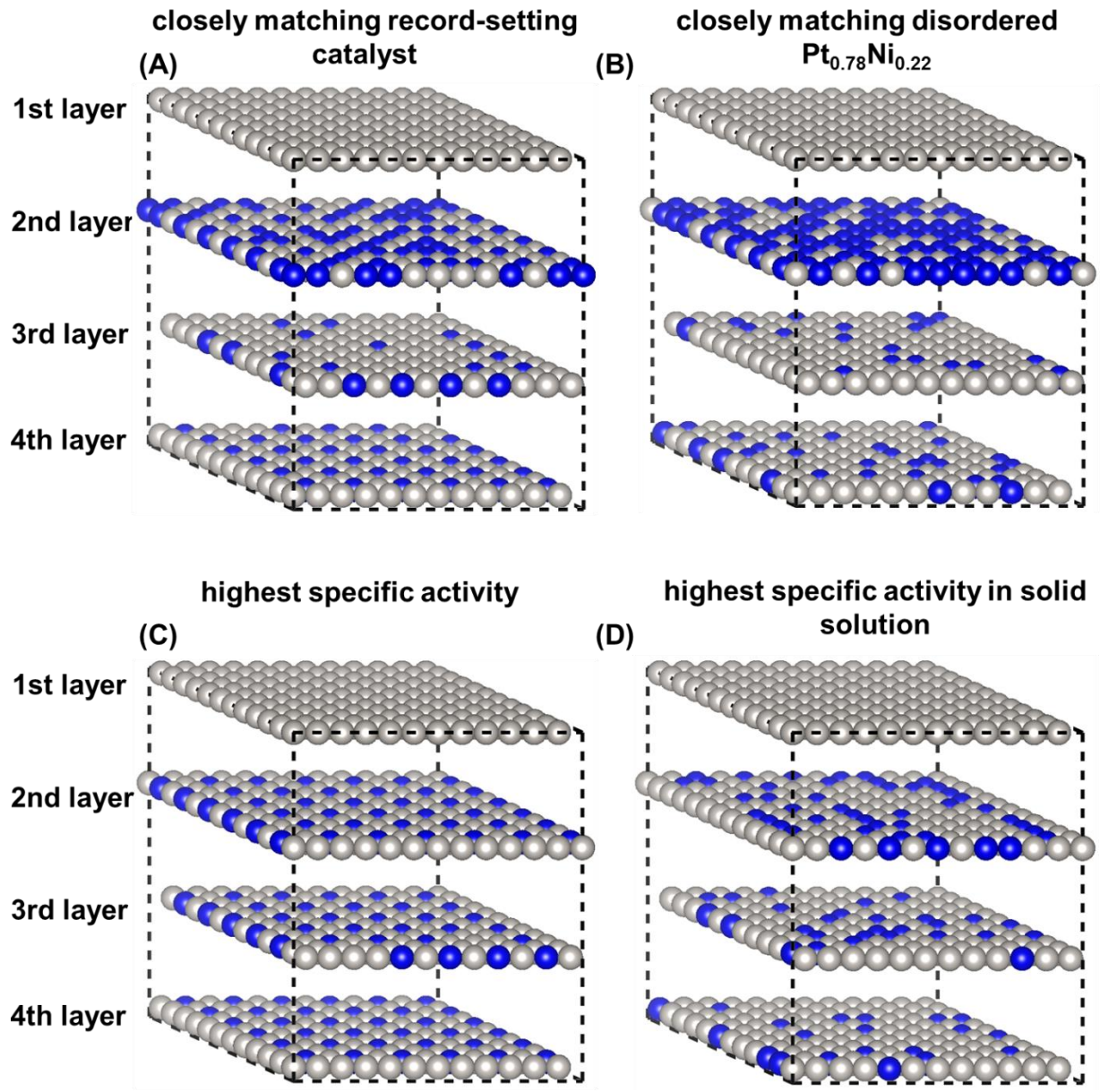

Fig. S5. Side views of the first, second, third and fourth layers for three representative snapshot slabs with a 12 × 12 (111) unit cell from Monte Carlo simulations. (A) A snapshot of a surface at a temperature of 420 K and a bulk Pt composition of 76.9% with a similar layer-by-layer composition profile as the record-setting catalyst reported by Stamenkovic et al. (10); (B) a snapshot of a surface at a temperature of 600 K and a bulk Pt composition of 77.5% with a similar layer-by-layer composition profile as the disordered $Pt_{0.78}$ $Ni_{0.22}$ alloy reported in reference (11); (C) a snapshot of a surface with highest predicted specific activity at a temperature of 240 K and a bulk Pt composition of 75.5%; and (D) a snapshot of a surface with the highest predicted specific activity in the solid-solution region at a temperature of 1200 K and a bulk Pt composition of 85.4%. The top views of the 2nd layer of figures A, C, and D are shown in the main text in Fig. 5 E, C, and D respectively.

2.6 Coverage-dependent catalytic activity maps predicted by kinetic Monte Carlo

To estimate how surface coverage affects catalytic activity, we have used an approach in which the turnover frequency at each site is determined through a kinetic Monte Carlo (KMC) simulation rather than directly using the oxygen adsorption energy at ¼ ML in a Sabatier volcano. We note that this provides only an estimate of coverage effects, as other species (such as OH) are likely to be present on the surface. To calculate the current using KMC, we ran a KMC simulation after each successfully completed step (i.e. change in Pt/Ni site occupancy) in the Metropolis Monte Carlo simulations described in section 2.5. Thus for each point on the catalytic activity map there is an inner loop that calculates the current for each atomic arrangement and an outer loop that averages the current over atomic arrangements. Each KMC simulation used 2,000 equilibration steps and 2,000 recording steps, and the values of predicted KMC currents were averaged over 50 independent parallel runs.

We use a standard "rejection-free" KMC algorithm (12, 13) in which the only allowed transitions are adsorption and desorption. All simulations were done using a 12 × 12 (111) supercell, so there are always 144 possible transition events for each KMC step. The rates for the transition events were calculated as $e^{\frac{-E_a}{kT}}$, where the effective activation energy, E_a, is calculated using the of Sabatier volcano. Specifically, for an adsorption event,

$$E_a = 0.297 + \max(0,\ 0.53(\Delta E_O - 1.699)), \quad [7]$$

where 1.699 is the peak position ($\Delta E_{O,\,peak}$=1.699 eV) of the volcano plot. For a desorption event,

$$E_a = 0.297 + \max(0,\ 0.5(1.699 - \Delta E_O)). \quad [8]$$

The maximum of E_a for an adsorption and an desorption event reproduces the equation of the Sabatier volcano plot (Eq. [4]) for the ORR along the reaction pathway of the associative mechanism. After each event, the total elapsed "KMC time" was incremented by

$$\Delta t = \left(\frac{1}{R_N} \right) * \ln \left(\frac{1}{u_1} \right) \quad [9]$$

where R_N is the total rate that sum all possible transition events, and u_1 is a uniform random number with $\mu_1 \in (0,1]$. At the end of the run, the ORR current was then calculated using

$$\langle I \rangle_{\mathrm{KMC}} = I_0 \left(\frac{\mathrm{n(accepted\ desorption\ events)}}{t_{\mathrm{KMC}}} \right) \quad [10]$$

where I_0 is a prefactor, $\mathrm{n(accepted\ desorption\ events)}$ is the number of accepted oxygen desorption events, and t_{KMC} is the "KMC time". When I_0 is the inverse of the number of adsorption sites per simulation cell (i.e. 1/144), then the KMC current agrees with the current calculated from the Sabatier volcano (Equation [6]) in the limit of dilute coverage.

The resultant KMC-predicted current maps (Fig. S6A) shows a similar trend to the one generated using the Sabatier volcano plot (Fig. 2A): the region of highest catalytic activity is on the Pt-rich side of the ordered Pt_3Ni phase, and there is another region of high catalytic activity for more Pt-rich compositions in solid solutions. The maximum currents are below those observed experimentally, which we believe is likely primarily due our assumption that O is the only species present when calculating the coverage effect.

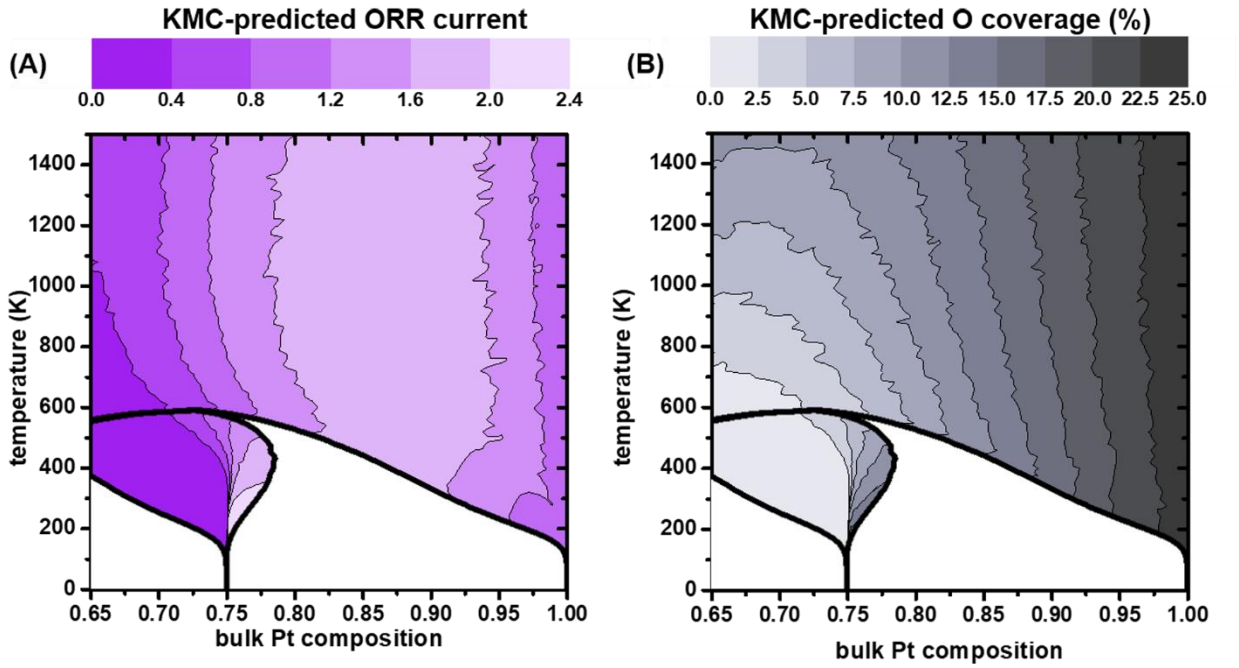

Fig. S6. (A) KMC-calculated coverage-dependent catalytic activity maps on slabs as a function of bulk Pt composition and temperature. The KMC-predicted currents are referenced to the KMC-predicted current on pure Pt(111). (B) A map of average oxygen coverage from the KMC simulations. In both (A) and (B) the calculated bulk phase diagram from Fig. 1 has been overlaid.

3. Simulations of metastable solid solutions

To examine the catalytic activity of metastable Pt–Ni solid solutions, we constructed a model in which we assumed that bulk alloy was kinetically frozen in its solid solution structure at 600 K, and the surface of the alloy was in thermodynamic equilibrium with the bulk solid solution. Determining the structure of a slab that is in equilibrium with the bulk requires knowledge of the chemical potential of the elements in the solution, which cannot be accessed directly by Monte Carlo simulations. To calculate the chemical potentials of the metastable phases, we first calculated the entropic contribution to the chemical potential of the stable phase at 600 K by subtracting the energetic contribution from the chemical potential:

$$\mu_{entropy}(600) = \mu(600) - \mu_{energy}(600), \quad [11]$$

where the energetic contribution to the chemical potential at 600 K is defined as

$$\mu_{energy}(600) = \frac{\partial E_f(600)}{\partial x_{Pt}}, \quad [12]$$

where E_f is the average formation energy per atom and x_{Pt} is the mole fraction of Pt. The derivatives were calculated using finite differences of well-converged Monte Carlo calculations at 600 K. We found that the entropic contributions to the chemical potentials calculated this way were slightly less than those that would be predicted in an ideal solution model, in good agreement with theory. At a general temperature of T, the chemical potential of the metastable solid solution is then given by:

$$\mu(T) = \mu_{energy}(600) + \frac{T}{600}\mu_{entropy}(600). \quad [13]$$

A comparison of the chemical potentials for the thermodynamically stable structures and the metastable structures as a function of composition and temperature is provided in Fig. S7. To identify a lowest-energy slab for each adjusted μ at 0 K, we ran Monte Carlo simulations by cooling down from 600 K to 0 K with chemical potential adjusted according to Eq. [13] at each temperature to obtain a list of candidate low-energy slabs at 0 K. Then for each adjusted μ at 0 K and the underlying bulk Pt composition in solid solution, we calculated the energies of all those candidate slabs to identify the slab with lowest CE-predicted energy at 0 K, which was used in the

Monte Carlo simulations of heating up from 0 K to 600 K. The predicted composition profiles and ORR current in metastable solid solutions are provided in Fig. S8 and Fig. S9.

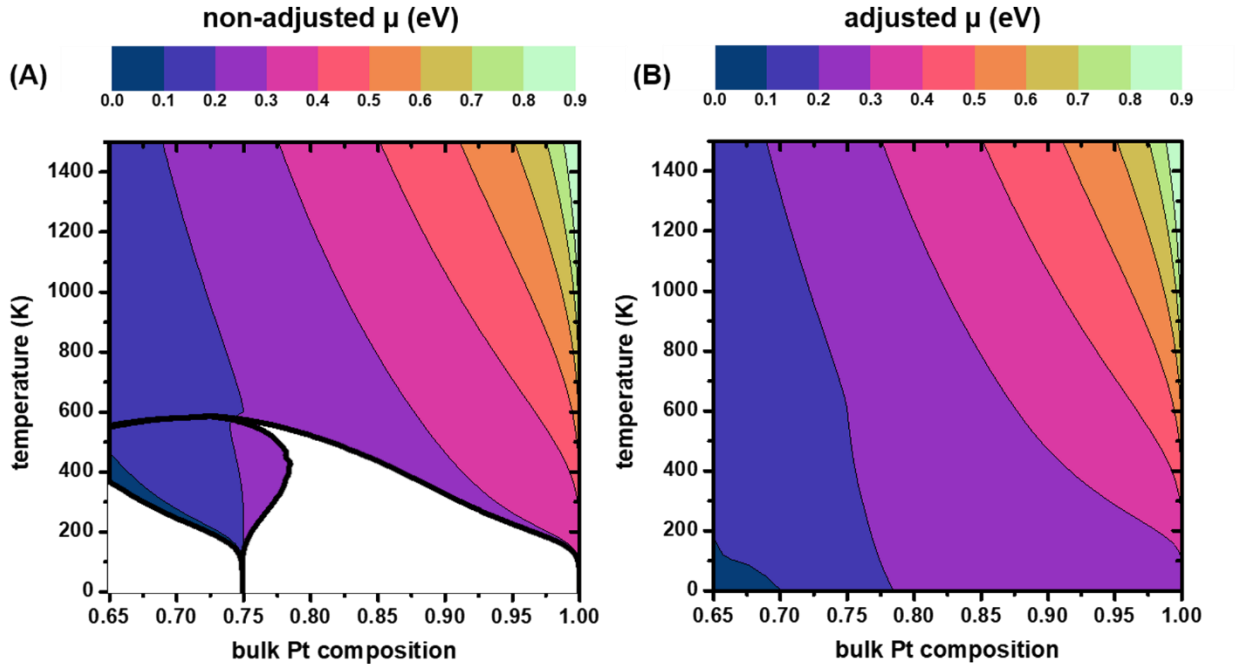

Fig. S7. Chemical potentials (μ) for (A) the thermodynamically stable structures and (B) the metastable structures as a function of bulk Pt composition and temperature.

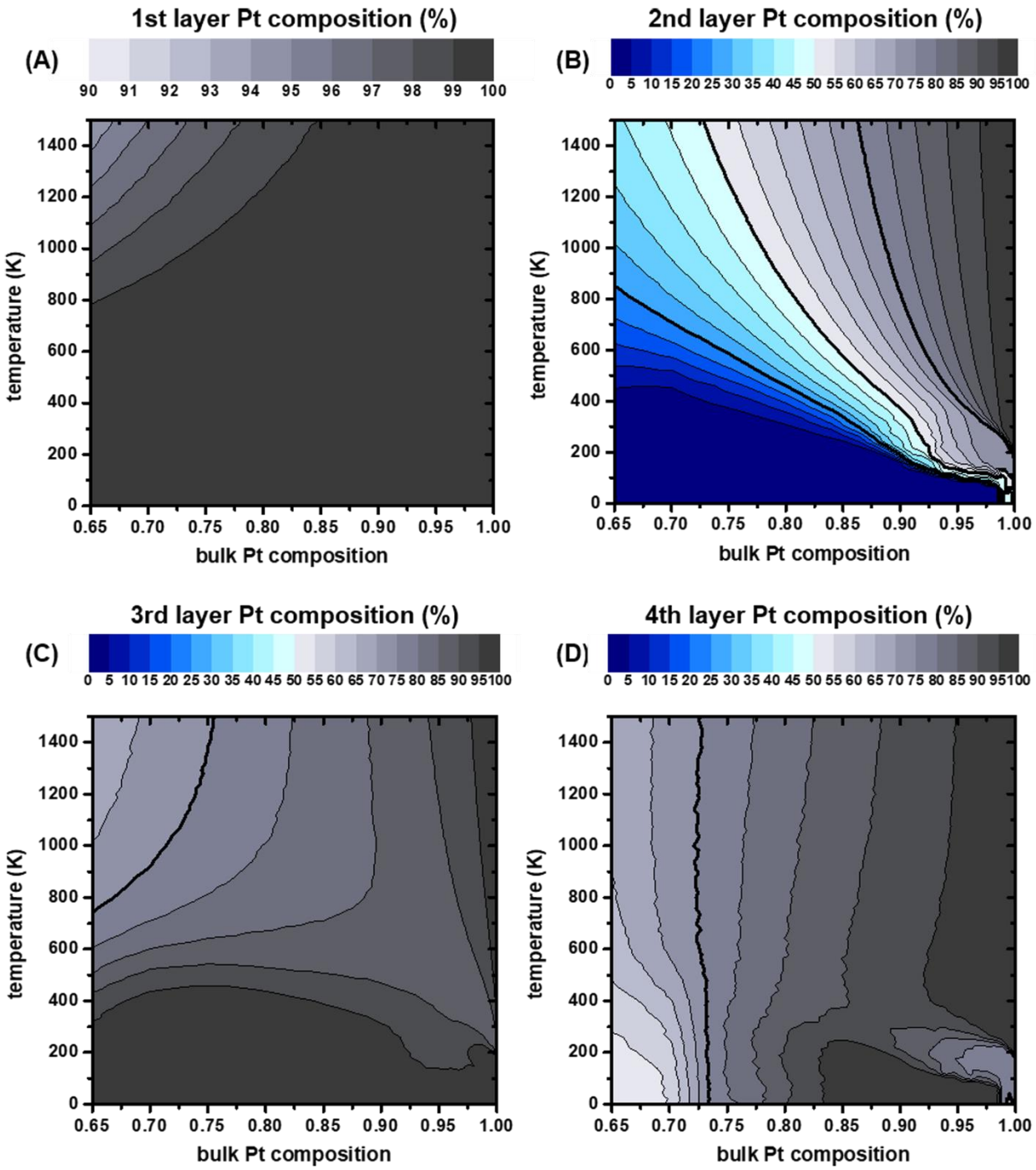

Fig. S8. Layer-by-layer composition maps on slabs in metastable solid solutions. The predicted Pt compositions in the (A) first, (B) second, (D) third, and (D) fourth layers of Pt–Ni(111) surfaces as a function of bulk Pt composition and temperature. Thick black lines mark Pt compositions that are multiples of 0.25.

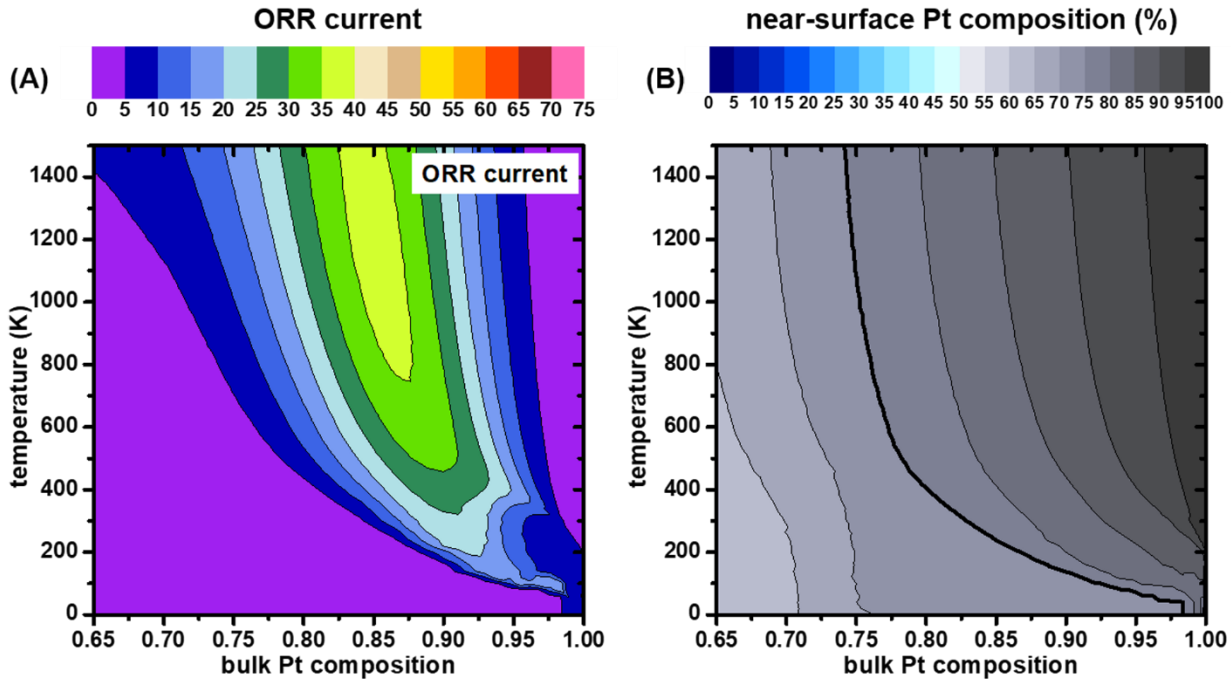

Fig. S9. Catalytic activity and near-surface composition maps on slabs in metastable solid solutions. (A) The predicted average ORR currents relative to Pt(111) and (B) near-surface Pt composition on Pt–Ni(111) surfaces as a function of bulk Pt composition and temperature. Thick black lines mark Pt compositions that are multiples of 0.25.

4. Chemical potential and bulk composition

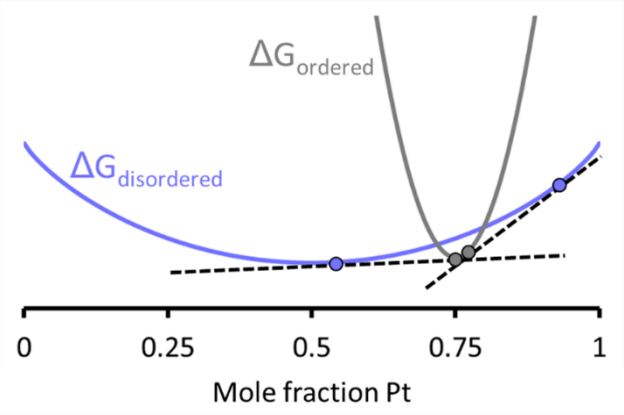

Fig. S10. A schematic of free energy curves for ordered (grey) and disordered (blue) phases. The value of μ (defined in Eq. [4] in the main body) at each point on the curve equals the slope of the curve, and the dashed black lines are common tangent lines between the curves, with the tangent points marked by small circles. The same range of μ values are covered over a small composition range in the ordered phase (between the two grey circles) as in a much wider composition range in the disordered phase (between the two blue circles).

5. Sensitivity of our model to changes

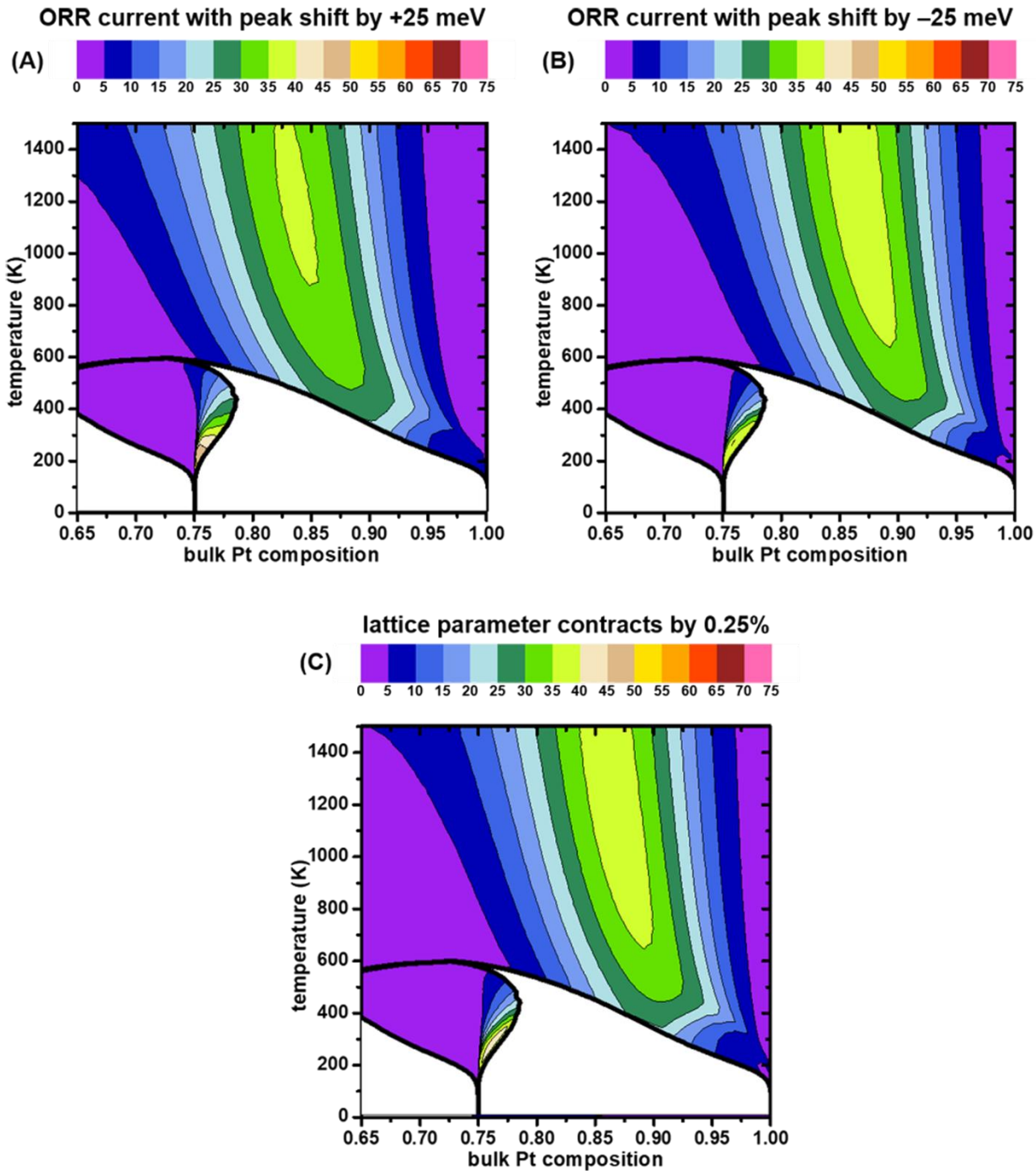

Fig. S11. Catalytic activity maps on slabs under three types of constraints as a function of bulk Pt composition and temperature. The peak of volcano plot has been shifted by (A) +25 meV (weaker *O binding) and (b) –25 meV (stronger *O binding). In (C) the lattice parameters at all points have been contracted by 0.25% as might occur in a 5 nm nanoparticle (14). The calculated bulk phase diagram in Fig. 1 has been overlaid on figures A-C.

References

1. Mueller T & Ceder G (2009) Bayesian Approach to Cluster Expansions. *Phys. Rev. B* 80:024103.
2. Mueller T & Ceder G (2010) Exact Expressions for Structure Selection in Cluster Expansions. *Phys. Rev. B* 82(Copyright (C) 2015 American Chemical Society (ACS). All Rights Reserved.):184107.
3. Van de Walle A & Ceder G (2002) Automating First-Principles Phase Diagram Calculations. *J. Phase Equilib.* 23:348-359.
4. Cao L & Mueller T (2015) Rational Design of Pt_3Ni Surface Structures for the Oxygen Reduction Reaction. *J. Phys. Chem. C* 119(31):17735-17747.
5. van de Walle A, Asta M, & Ceder G (2002) The alloy theoretic automated toolkit: A user guide. *CALPHAD* 26(4):539-553.
6. van de Walle A & Asta M (2002) Self-driven lattice-model Monte Carlo simulations of alloy thermodynamic properties and phase diagrams. *Modell. Simul. Mater. Sci. Eng.* 10(5):521-538.
7. van de Walle A (2009) Multicomponent multisublattice alloys, nonconfigurational entropy and other additions to the Alloy Theoretic Automated Toolkit. *Calphad* 33(2):266-278.
8. Karlberg GS, Rossmeisl J, & Norskov JK (2007) Estimations of Electric Field Effects on the Oxygen Reduction Reaction based on the Density Functional Theory. *Phys. Chem. Chem. Phys.* 9:5158-5161.
9. Norskov JK*, et al.* (2004) Origin of the Overpotential for Oxygen Reduction at a Fuel-Cell Cathode. *J. Phys. Chem. B* 108:17886-17892.
10. Stamenkovic VR*, et al.* (2007) Improved Oxygen Reduction Activity on $Pt_3Ni(111)$ via Increased Surface Site Availability. *Science* 315:493-497.
11. Gauthier Y, Joly Y, Baudoing R, & Rundgren J (1985) Surface-sandwich segregation on nondilute bimetallic alloys: $Pt_{50}Ni_{50}$ and $Pt_{78}Ni_{22}$ probed by low-energy electron diffraction. *Phys. Rev. B* 31(10):6216-6218.
12. Schulze TP (2008) Efficient kinetic Monte Carlo simulation. *J. Comput. Phys.* 227(4):2455-2462.
13. Serebrinsky SA (2011) Physical Time Scale in Kinetic Monte Carlo Simulations of Continuous-Time Markov Chains. *Phys. Rev. E* 83(3):037701.
14. Leontyev IN*, et al.* (2014) Size dependence of the lattice parameters of carbon supported platinum nanoparticles: X-ray diffraction analysis and theoretical considerations. *RSC Adv.* 4(68):35959-35965.